Lawrence Berkeley National Laboratory

Title

Multidimensional, Experimental, and Modeling Evaluation of Permeability Evolution, The Caney Shale Field Lab, OK, USA

Permalink

https://escholarship.org/uc/item/4hd6w9fp

Authors

Katende, Allan
Awejori, Gabriel
Benge, Margaret
et al.

Publication Date

2023

DOI

10.15530/urtec-2023-3869822

Peer reviewed

URTeC: 3869822

Multidimensional, experimental and modeling evaluation of permeability evolution, the Caney Shale Field Lab, OK, USA

A. Katende[1,2], G. Awejori[1,2], M. Benge[5], S. Nakagawa[4], Y. Wang[3], F. Xiong[1,2], J. Puckette[3], M. Grammer[3], J. Rutqvist[4],C. Doughty[4], A. Bunger[5], T. Paronish[6], D. Crandall[6], J. Renk[6] and M. Radonjic[1,2,3,*]

[1]Hydraulic Barrier Materials and Materials Characterization Laboratories, 126, 127 & 130, Advanced Technology Research Center(ATRC), Oklahoma State University, Stillwater, OK 74078, United States of America(USA)
[2]School of Chemical Engineering, Oklahoma State University; 420 Engineering North, Stillwater, OK 74078, USA
[3]Boone Pickens School of Geology, Oklahoma State University, Stillwater, OK 74078, United States of America(USA)
[4]Energy Geosciences Division, Lawrence Berkeley National Laboratory, 1 Cyclotron Road, Berkeley, CA 94720, USA
[5]Department of Civil and Environmental Engineering, University of Pittsburgh, Pittsburgh, PA 15260, United States of America(USA)
[6]National Energy Technology Laboratory, Research and Innovation Center, Morgantown, WV 26505, United States of America(USA)

Abstract

A key feature of unconventional shale reservoirs is low permeability. On average, only 10% of original oil in place and 25% of original gas in place is produced from these reservoirs. Understanding the mechanisms behind fracture conductivity past the first couple of years of shale production is still an ongoing research topic, as most such reservoirs report fast and massive production declines. Hydraulic fracturing is indispensable for stimulating low-permeability rocks for economical oil and gas production from unconventional reservoir rocks such as shales. In contrast, for subsurface sequestration and storage of fluids including supercritical CO_2 (for carbon capture, utilization, and storage) and hydrogen gas, inadvertent creation of fractures can lead to breaching of shale caprock. The Caney Shale in southern Oklahoma is being evaluated as both a potential hydrocarbon-producing reservoir and a caprock for fluid sequestration. The Caney Shale is a Mississippian-age, organic-rich mudrock with intermittent calcareous laminae, that produces. But currently there is limited data reported regarding productivity of horizontally drilled wellbores. While many scholars have investigated fracture conductivity in shale reservoirs, the mechanisms of proppant embedment in relation to lithology are still under investigation. This study implemented a multi-scale approach towards investigating proppant embedment and fracture conductivity, from nano-scale instrumented micro/nano-indentation to millimeter (mm) scale, mono-layer propped fracture flow at reservoir temperature and pressure, and American Petroleum Institute (API)-RP19D conductivity tests using inch/cm-scale shale platens. At each scale, various material characterization tools were utilized, including Focused Ion Beam-Scanning Electron Microscopy (FIB-SEM), Energy Dispersive Spectroscopy (EDS), Raman spectroscopy, Laser profilometry, Computed X-ray Microscopy and X-ray Diffraction (XRD). The outcomes of the micro-indentation revealed variations in mechanical properties attributed to changing mineral composition and microstructures. Outcomes from API fracture conductivity testing and flow- through testing using a monolayer of proppant demonstrated: (1) a 50% impact on proppant embedment compared to ductile samples, (2) a significant decline in fracture conductivity with increasing stress and temperatures, and (3) conductivity that was also influenced by organic and inorganic content as well as internal sample architecture. Mineralogically, ductile samples contain about 25% more clay minerals compared to brittle regions. Heterogeneity in mineral composition causes the Caney Shale to show different responses at reservoir temperature and pressure, particularly in relation to creep and proppant embedment. Geomechanical and fluid-flow modeling have been conducted at several scales to help interpret laboratory results and apply findings to field-scale operation. The outcomes from this integration should aid geological and engineering predictions for the hydrocarbon production and caprock integrity of the Caney Shale.

Introduction

The pivot towards shale gas production in the United States has had a significant transformative effect on the global energy structure (Wang et al., 2014; Katende et al., 2023b). It has also accelerated the theoretical understanding, technological development, and explorative efforts in the field of oil and gas. Recent research on shale gas has focused in particular on the lithological nature and depositional environment of sites, or has sought to evaluate the shale gas resources available. The distinguishing features of shale gas systems include seals with various lithological characteristics, intricate trapping mechanisms, etc. (Lee et al., 2011).

Together with silts, shales represent one of the most common sedimentary rocks. Based on recent production trends, shale gas is likely to become the most significant component of global gas production. However, shale gas reservoirs differ from conventional reservoirs due to their extremely low permeability; consequently, they must be fractured hydraulically in order for the gas extraction to be commercially profitable. Hydraulic fracturing and horizontal drilling are important techniques that are expected to continue to advance in the future. With the ability to explore and exploit unconventional reservoirs relying significantly on hydraulic fracturing technologies, it should be noted that a reservoir's performance substantially influenced by its shale heterogeneity and anisotropy, which in turn are shaped by the local mineralogical and mechanical aspects of the formation (Clarkson et al., 2011, 2013; Katende et al., 2021a,b, 2023a,b).

Using discrete element modeling, Liuke et al. (2019) examined how the inherent heterogeneity and grain size of the rocks affect hydraulic fracturing performance. Specifically, they utilized random particle assembly to numerically model the inherent heterogeneity of the rock, against a reference comprising regular particle assembly. They revealed that in the viscosity-dominated regime, the inherent heterogeneity of the rock primarily influences the hydraulic fracture net pressure, although in the toughness-dominated regime this effect is stronger. Meanwhile, the study by Dou et al. (2019) highlighted the importance of the bedding planes' tensile strength-shear strength relationship as it contributes to shale slip failure and is closely linked to the fluid flow network's complexity.

Furthermore, the hydraulic performance of a shale gas reservoir is substantially influenced by its underlying sedimentation processes as these affect the site's mineral components (Loucks et al., 2012; Wang et al., 2021). There are a number of ways to examine the micro structural and mineral components in sedimentary shale rocks, such as optical microscopy and scanning electron microscopy (Radonjic et al., 2020), x-ray diffraction analysis (Awejori et al., 2021), and x-ray computed tomography (Paronish et al., 2021). Investigating the mineral components of shale, Ding et al. (2012) revealed that organic carbon, clay minerals such as kaolinite, illite, and montmorillonite, and clastic and authigenic minerals such as mica, quartz, feldspar, and calcite are the main constituents in most shales. Finally, according to (Benge et al., 2021), although shale formations can share similar mineral compositions, their mechanical properties can vary widely.

For instance, Xu et al. (2020) analyzed samples from Jiaoshiba block shale to ascertain whether the mineral composition affected the elastic modulus. The authors found that differences in the mineral components affect the mechanical properties, which in turn have a considerable effect on hydraulic fracturing performance. In a similar way, Guo et al. (2019) revealed a difference between shales with high and low brittleness: While the former are characterized by a split fracture plane that predominantly experiences tensile failure, a single shear fracture plane occurs with the latter. Furthermore, it has been established that shales with proportionally more brittle components are more likely to have tree-like fracture networks, increasing the number of flow paths for the shale gas(Rutqvist et al., 2013; Guo et al., 2015).
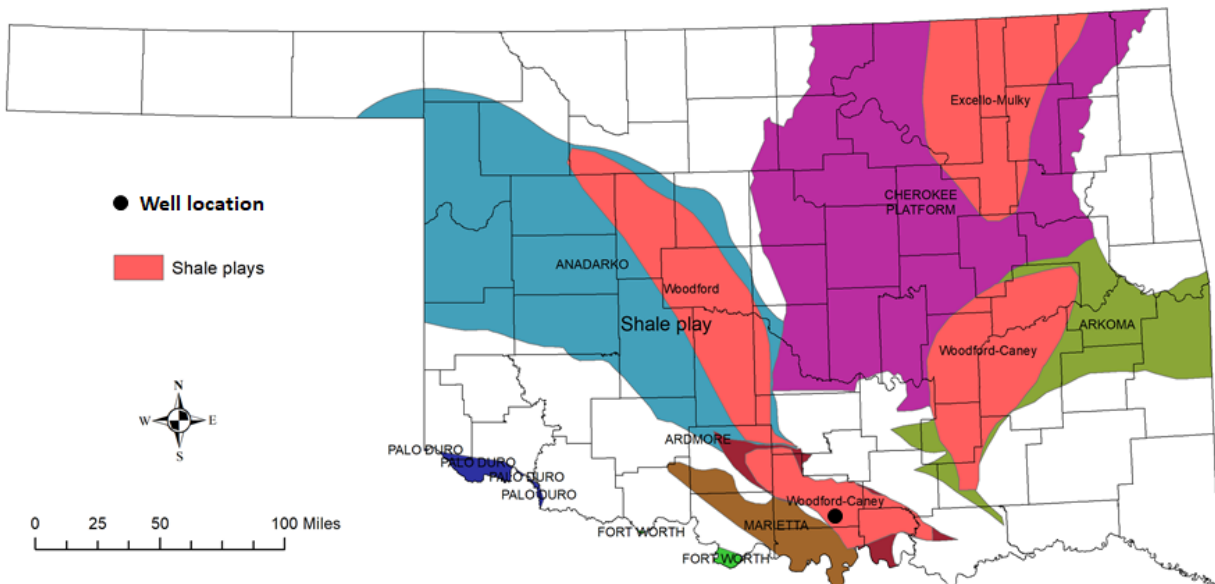

Figure 1: Shale plays as their associated geological basins in Oklahoma. The well(black dot on map) of this study is located within the Ardmore Basin in southwest Oklahoma ,USA.
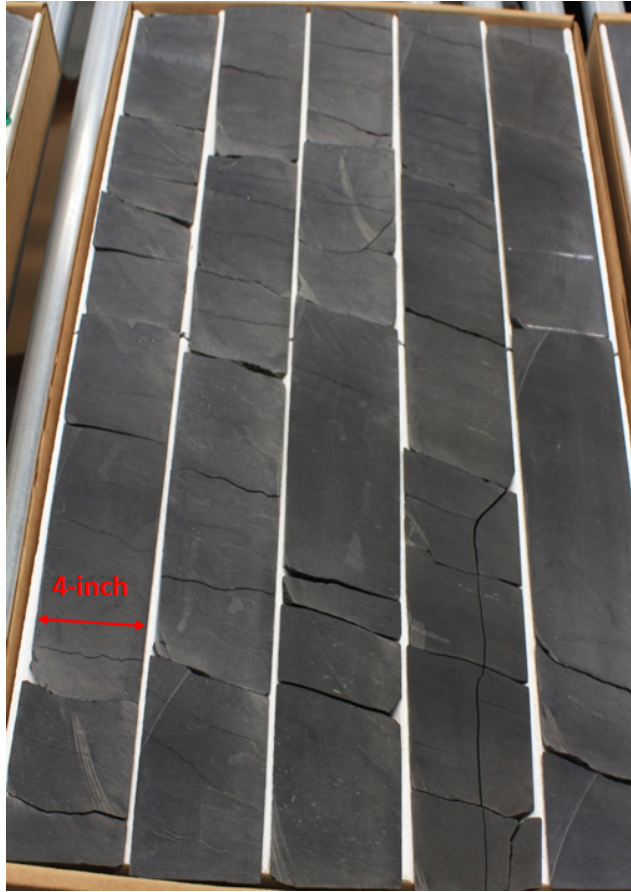
Figure 2: A digital photograph representation box of the Caney shale. One third lengthwise sliced for viewing and record keeping and two thirds remainder of the core was used to drill core plugs for analysis. Some of the visual observations are laminations due to separation and drying(Phosphates and Carbonates) and the entire core is dominated by a dark rich black shale.

The late Mississippian Caney Shale formation has been recognized as an emerging unconventional hydrocarbon resource play in the US Mid-continent region. Mostly found in southern Oklahoma, the subsurface Caney Shale is present in the Ardmore and Arkoma basins (Figure. 1), and based on limited publication records (e.g., Kamann (2006)), contains "shale" (or organic-rich, calcareous, siliceous, and silty mudstone) with siltstone and carbonate intervals. Figure. 2, shows a digital photograph representation box of the Caney shale. One third lengthwise sliced for viewing and record keeping and two thirds remainder of the core was used to drill core plugs for analysis. Some of the visual observations are laminations due to separation and drying(Phosphates and Carbonates) and the entire core is dominated by a dark rich black shale. Despite having a history dating back to early 2000s (Andrews, 2007), production from the Caney Shale has been relatively sparse and unpredictable (e.g., Andrews (2007); Cardott (2017)). In addition, published studies that focus on an integration among core, log, and field data for understanding the production potential and reservoir distribution of the Caney

Shale seem lacking.

Contribution

The Caney Shale in southern Oklahoma is being evaluated as both a potential hydrocarbon-producing reservoir and a caprock for carbon dioxide sequestration. The Caney Shale is a Mississippian-age, organic-rich, often calcareous mudrock, that produces oil and gas. But currently there is limited data reported regarding productivity of horizontally drilled wellbores in the Caney shale and while many scholars have investigated fracture conductivity in shale reservoirs, the mechanisms of proppant embedment in relation to lithology are still being studied and or particular importance to more ductile rocks like the Caney shale.

Methodology

This study has implemented a multi-scale approach towards investigating proppant embedment and fracture conductivity, from nano-scale instrumented micro/nano-indentation to millimeter (mm) scale, mono-layer propped fracture flow at reservoir temperature and pressure, and American Petroleum Institute (API)-RP19D conductivity tests using inch/cm-scale shale platens At each scale, various material characterization tools were utilized, including Focused Ion Beam-Scanning Electron Microscopy (FIB-SEM), Energy Dispersive Spectrum (EDS), Raman spectroscopy, Laser profilometry, Computed X-ray Microscopy and X-ray Diffraction (XRD). By increasing our understanding of the properties of the Caney Shale that allow it to be a self-contained petroleum system with source, reservoirs and seals, we are able to extend these findings to other areas containing the Caney Shale, as well as increase our understanding of more ductile shales in other basins.

Sample Selection   Caney shale samples which were cored while drilling a well in January 2020 have been used in this study. About 650-feet of core was retrieved while drilling an exploratory well and Table 1 shows the depth of the intervals used in this study.

Table 1: Caney shale selected rock samples from the 650feet of drilled core

Well Depth (ft)	Formation Description
X006	Sample A (Reservoir 1-R1)
X087	Sample B (Ductile 1-D1)
X139	Sample C (Reservoir 2-R2)
X171	Sample D (Ductile 2-D2)
X404	Sample E (Reservoir 3-R3)

Computed Tomography Scanning   The entire length of the 2/3rd slabbed section of the Caney shale well was scanned using the U.S. Department of Energy National Energy Technology Laboratory's (NETL's) Toshiba Aquilion TSX-101A/R medical computed tomography scanner. Scans were acquired at 135 kV and 200 mA (high energy) and 80 kV and 200 mA (low energy) with a voxel resolution of 0.43 mm x 0.43 mm across the diameter of the core and 0.50 mm along the length of the core. High and low energy CT scanning enabled the calculation of dual-energy density of the cores along its length. Variations in composition, such as open fractures and the location of high-density inclusions, can be directly observed in the high energy medical CT scans. One hundred core plugs along the length of this core were scanned with the medical CT scanner as well to determine internal features of these samples prior to further testing. Higher resolution industrial CT scans of nine sections of the core were acquired with NETL's North Star Imaging Inc. M-5000 Industrial Computed Tomography System where features of interest were identified to complement this continuous data, with voxel resolutions ranging from $(40\mu m)^3$ to $(100\mu m)^3$, depending on the size of the section scanned. All raw CT data and select processed images are publicly available on the Energy Data eXchange(EDeX) and described in a complementary technical report (Paronish et al., 2021).

Additional CT scanning was done using an YXLON FF20 Industrial CT scan in the hydraulic barrier and materials characterization laboratory at Oklahoma State University. Cores were scanned at submillimeter resolution using a voltage of 175kV and a current of 70mA.

Porosity/Permeability   Porosity for the samples in our study was determined with the aid of Argon gas. Dry grain density was measured, then argon gas was introduced and grain density and bulk density were determined. Porosity was then calculated by dividing the pore volume with the bulk volume. Permeability was determined using a pulse decay permeameter on samples that were as received and samples that were cleaned with Carbondioxide (CO_2) and Toluene$(C_6H_5CH_3)$.

X-ray Diffraction (XRD)   Samples used for XRD measurements were powdered samples prepared from recovered cored rock. To prepare samples, rocks were crushed and grounded to particle sizes passing 140 mesh size $(100\mu m)$ using ball mill and microne micronizer. Mineralogical composition of rocks helps to understand the make-up of the rock and how this rock responds to fluids or stresses in the subsurface. XRD analyses were conducted on rock-powder of samples to ascertain their compositions. The Bruker D8 Advanced X-ray Diffractometer with a Lynxeye detector was used for XRD measurements. Scanning was done for 2-theta angles between 5 to 80 degrees at 0.01 degree steps and dwell time of 0.5 seconds. Semi-quantitative analyses were undertaken on the results using the Diffrac.suite eva software to obtain the mineralogical composition of samples.

X-ray Fluorescence (XRF)   Data necessary for the success of this research were acquired from a core that captured the entire Caney Shale. This core was described and sampled for a number of different analyses to determine geological and geomechanical properties including Tight Rock Analysis (TRA) that provided grain density, porosity and permeability measurements, Source Rock Analysis (SRA) that examined kerogen type, maturity and TOC, X-ray diffraction (XRD) to establish mineralogy, and X-ray fluorescence (XRF) to determine elemental concentrations and evaluate redox conditions and paleo productivity during deposition (Tribovillard et al., 2006; Algeo and Maynard, 2004) and relative changes in marine and terrigenous sediment supply during Caney deposition. In addition, the core was scanned using Computed Tomography (CT) to visualize internal features and sampled for scanning electron microscopy (SEM) and a series of geomechanical tests including creep tests and indentation testing.

Geophysical measurements along the entire length of the 2/3rd slabbed core of the Caney shale well was obtained using NETL's Geotek Multi-Sensor Core Logger. With 6 cm spacing measurements of magnetic susceptibility, P-wave velocity, and gamma density were collected. Magnetic susceptibility can be used to indicate presence of paramagnetic and diamagnetic materials e.g., iron and calcite respectively. P-wave measurements illustrate the ability for compressional waves to transmit through the core and are higher with denser and more competent sections. Gamma density is acquired by exposing sections of the core to a gamma radiation source, measuring the attenuation of that radiation through the sample, and relating that attenuation to the bulk density of the sample. More details on the multi-sensor core logger methodologies can be found in Paronish et al. (2022). Coupled with the physical measurements from NETL's Geotek Multi-Sensor Core Logger, a handheld Innov-X X-Ray Fluorescence (XRF) Spectrometer was used to collect elemental information along the length of the core every 6 centimeters. Elements lighter than and including sodium were aggregated to one 'light element' measurement and 28 individual elements (Mg to Cl, K, Ca, Ti to Zn, As, Zr, Mo, Ag, Cd, Sn, Sb, Hf, W, Pb, and Bi) were recorded and reported in Paronish et al. (2021). Measurements were acquired using 60s exposure times with the "Mining-Plus Suite" on the Innov-X XRF Spectrometer to resolve these elements with 2-beam excitation.

Scanning Electron Microscopy/Energy Dispersive Spectroscopy(SEM/EDS) The geochemical and microstructural characterization of Caney Shale samples were carried out using a Scios 2 scanning electron microscope in the microscopy lab of Oklahoma State University. Backscattered electron mode with energy dispersive spectroscopy (EDS) is used for compositional characterization. The voltage and current of operation are set at 20kV and 0.8nA. The core sample was first polished using an Allied AD-5 MultiPrep system with water-free suspension and polishing cloth. Then the core sample was later ion milled with Ar using a JEOL IB-19500CP polisher.

Creep testing Creep testing was conducted using 30×60 mm cylindrical core plugs from each of the five identified zones. Testing consisted of using a Hoek type triaxial cell, allowing samples to be tested at 20.6 MPa and 90°C to simulate downhole conditions. Samples were loaded to 30% of their predetermined strength at 20.6 MPa confining pressure to avoid confusing sample damage for additional creep. Creep testing consisted of several load/recovery stages to monitor the creep and creep recovery of the samples over time. The test procedure consisted of a 24-hour hydrostatic stage, a 20-minute load cycle followed by a 20-minute relaxation stage, two 12-hour loading stages with a 12-hour relaxation stage between, a 2-hour relaxation stage, and a final 72-hour loading stage to examine long term creep behavior. For this paper, the 72-hour loading stage will be discussed.

Axial strain during creep testing was measured using three external LVDTs. To be able to compare samples with different axial loading, the creep compliance J was calculated by normalizing the creep strain(ε) by the applied differential stress(σ). To remove the influence of elastic strain and any creep which occurred prior to this loading stage, the creep strain was offset at the start of the 72-hour loading stage. The data was then fit to a power-law to predict the creep and provide a model for use in analyzing the creep compliance over time.

$$J = \frac{\varepsilon}{\sigma} = \frac{\varepsilon_{creep} - \varepsilon_{offset}}{\sigma} = B \times t^n \tag{1}$$

API Fracture permeability test vs single proppant layer fracture permeability test API fracture conductivity tests were conducted using an industry standard fracture conductivity cell and confining stresses were varied from 2000-psi(13.79MPa) to 10,000psi(68.95MPa) closing pressures using 2% KCl solution at 210°F (Katende et al., 2023a). Single layer fracture permeability tests were conducted using an Automated Core Flooding System(AFS) with a Caney shale composite consisting of 1-inch core specimens that were cored at different orientations to the bedding as described in Katende et al. (2023b). The experiment was conducted at reservoir conditions (Temperature of 125°C(257°F) and confining stressed up to 4011.82psi(27.66MPa), for a period of nine days.

In-situ fluorescence visualization(ISFV) of proppant and fracture aperture evolution A proppant crushing and embedment experiment was also conducted using an optical in-situ visualization system (**Figure. 3**). This system used a disc-shaped, clay-rich Caney shale sample (diameter=44.4 mm, thickness 6.4 mm). The disc served as an analogue fracture surface on which a sub-monolayer of proppant grains (1-1.5mm-size round quartz sand) was deposited, covering about 50% of the surface area. The shale disc (a "half fracture") and proppant were then compressed against a sapphire view window, mediated by a thin FEP film (thickness = 125 μm) and another sapphire disc, using an internal piston from the bottom of a confining cell. Brine mixed with a UV-fluorescent dye (WATER-GLO® 802-P, Spectroline) was injected into the test cell to image the proppant and fracture behavior through the window.
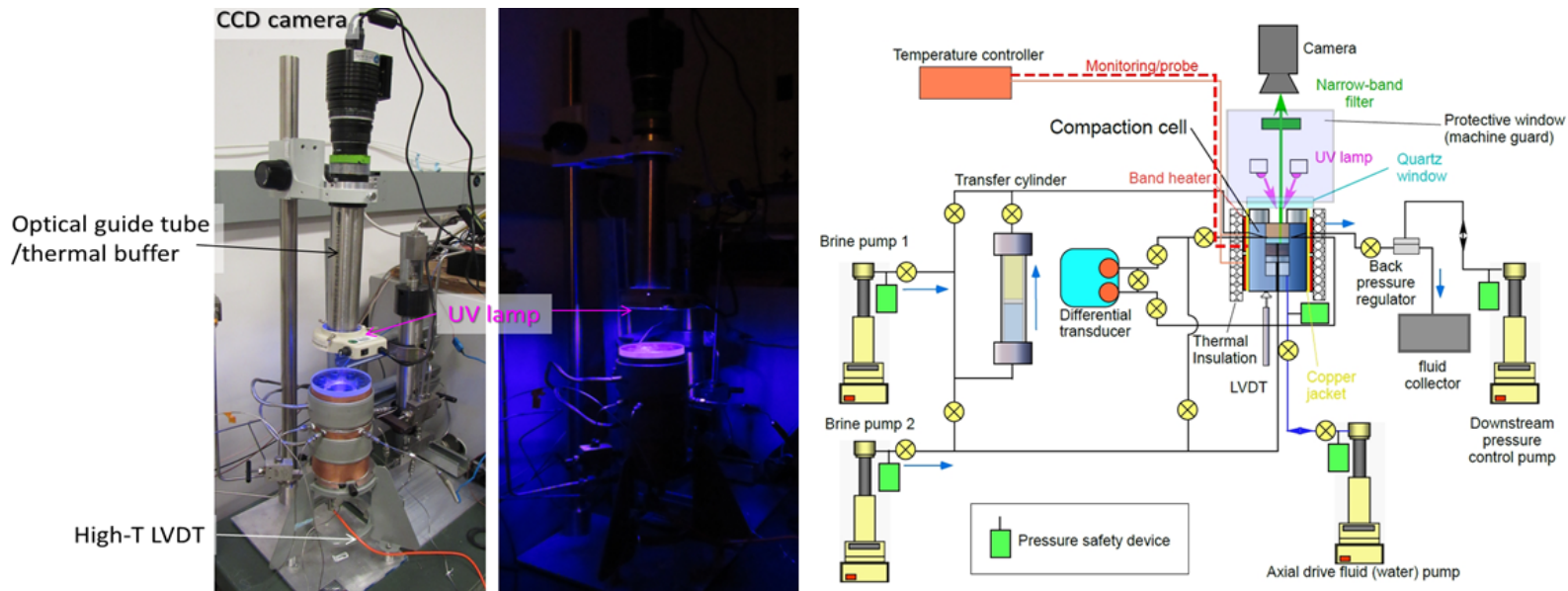

Figure 3: In-situ proppant-shale interaction visualization test system (Nakagawa and Borglin, 2019)

Micro/Nano Indenter A micro/nano indenter was used to determine the mechanical properties of the shale specimens identified which were then used to correlate to the susceptibility to proppant embedment by determining the hardness and elastic modulus of the samples. The experimental conditions used are those described in Katende et al. (2021a).

Total Organic Carbon analysis To determine the total organic carbon from the samples under analysis, the samples were first pulverized, and hydrochloric acid(HCl) was used to remove the carbon from the mineral matrix and thereafter samples were subjected to controlled heating for the determination of total organic carbon(TOC).

Modelling efforts The numerical modeling was performed considering an advanced multiphase fluid flow equation-of-state (Oldenburg et al., 2004) with plastic and visco-elastic (creep) constitutive models as required for ductile shales of high clay content. It was accomplished through TOUGH-FLAC, which is a coupled processes modeling framework, based on linking LBNL's TOUGH-family codes (Pruess, 2004; Pruess et al., 2012) to the FLAC3D geomechanics code (Rutqvist, 2017). Modeling was conducted at a range of scales from proppant scale to reservoir scale.

Table 2: Summary of the multidimensional workflow used in this study

Steps	Method/Technique	Purpose
	X-ray computed tomography (Large scale medical CT and large scale industrial CT). X-ray Fluorescence(XRF)	• To identify compositional heterogeneity, organic separation and chemical mineralogy
	Optical microscopy including SEM,FiB and EDS	• To study the millimeter microstructural characterization of micro fractures, grain boundaries and spatial distribution of clays and non clays
	Creep testing, Indentation testing and In-situ visualization of proppant for fracture aperture evolution	• Determine mechanical properties and identify rock susceptibility to proppant embedment
	Automated Flooding System for fracture permeability and API-RP 19D	• To determine fracture permeability for monolayer propped fractures and multilayer propped fractures
	Long term modeling of fracture permeability	• Identify and analyze how the well will perform in the forecasted future in relation to well productivity
INTEGRATION	**Integrate Wellbore scale plus chemistry, composition, heterogeneity of fractures at the microscale**	

Results

Caney shale at reservoir/wellbore scale: log data Conventional open wireline logs across the Caney Shale display characteristics associated with ductile clay-rich zones that are distinctly different than those associated with reservoirs, detrital clay- and silt-rich intervals or thin carbonates. Reservoirs, ductile zones, detrital zones and carbonates all exhibit different concentrations for selected elements as determined us x-ray fluorescence (XRF) (Figure 4). Ductile intervals have low resistivity values of <20 ohm-m, high neutron porosity of >24 porosity units and uncorrected density of 8 to 10 porosity units, and exhibit increasing detrital indicators Ti, Zr, Al and concurrent decreasing Si. In contrast, reservoirs intervals have higher resistivity of >400 ohm-m, lower neutron porosity of 18 to 20 porosity units and uncorrected density porosity values of 10 to 16 porosity units. Reservoirs have lower Ti, Zr, and Al concentrations along with higher Si. Detrital clay- and silt-rich intervals exhibit resistivity of <100 ohm-m, neutron porosity of around 20 porosity units and uncorrected density porosity of around 10 porosity units. Detrital silt- and clay-rich intervals show a concurrent increase in Ti, Zr, Al and Si that reflects the abundance of aluminosilicate clay minerals and detrital quartz. Carbonates have higher resistivity of > 100 ohm-m and very low neutron and density porosity (>6 porosity units). In carbonates, Ti, Zr, Al and Si are all at very low concentrations, but the concentration of Ca is high.
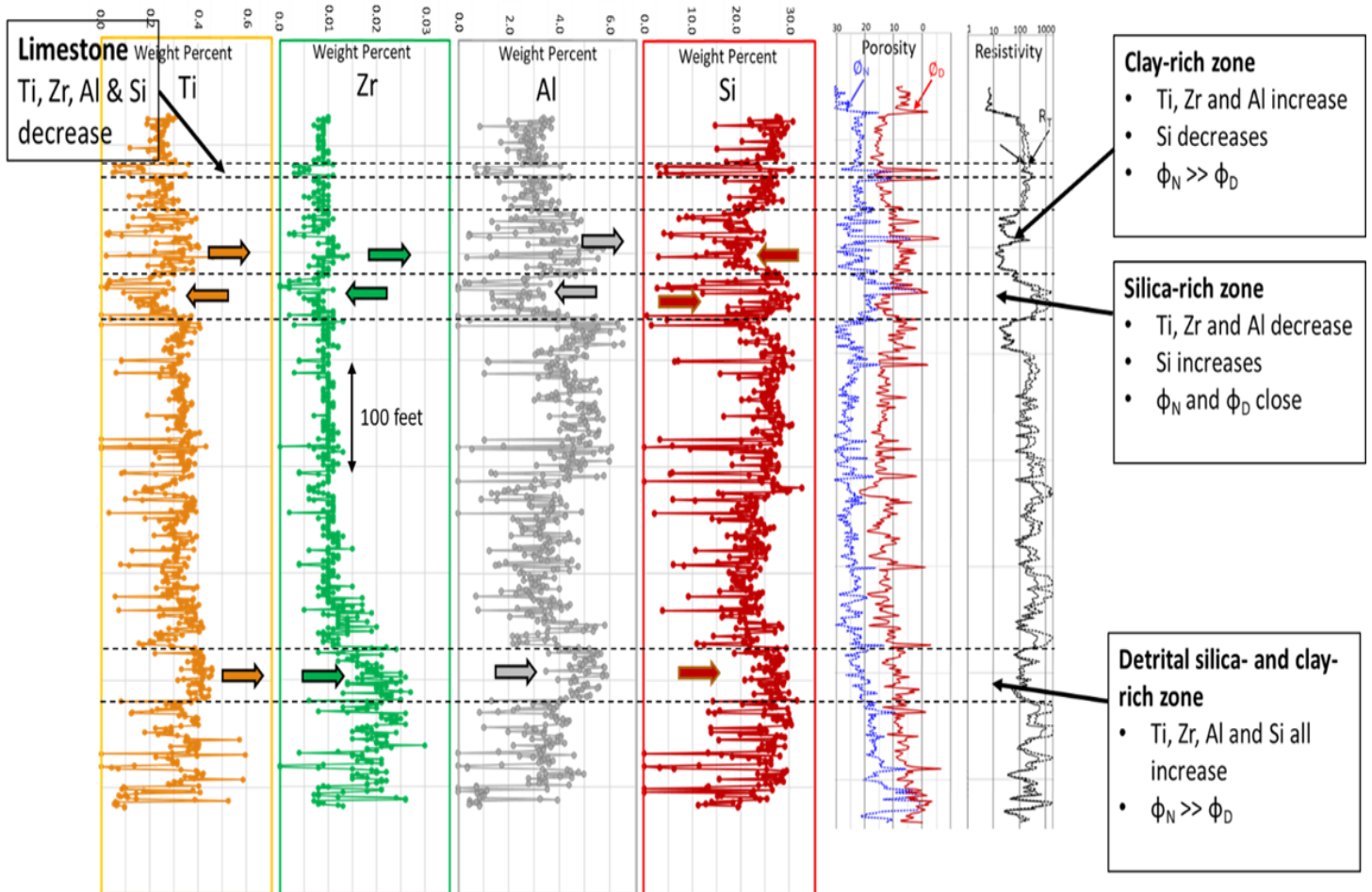

Figure 4: Concentrations of selected elements from XRF along with wireline log curves across the Caney Shale. Four distinct patterns are recognized: (1) intervals with decreasing Ti, Zr and Al, along with increasing Si, (2) intervals in which Ti, Zr and Al decrease, while Si increases, (3) intervals in which Ti, Zr, Al and Si all increase, and (4) intervals in which Ti, Zr, Al and Si decrease and Ca increases. Wireline log characteristics across interval 1 have lower resistivity, higher neutron porosity and lower uncorrected density porosity. Interval 2 exhibits higher resistivity, lower neutron porosity and higher density porosity. Interval 3 has wireline log characteristics similar to those for interval 1, whereas interval 4 has low concentrations of Ti, Zr, Al and Si, low neutron and density porosity along with higher resistivity.

Caney shale core data: Computed Tomography(CT), Total Organic Carbon(TOC), Porosity and Permeability

Computed Tomography (CT) The medical CT data of the Caney shale well was obtained with NETL's Toshiba Aquilion TSX-101A/R is available on the Energy Data eXchange (EDX) and described in a complementary technical report (Paronish et al., 2021). An example of these images in shown in Figure 5, where variations in the bedding planes in the shale along several hundred feet can be seen. With medical CT scanning smaller features such as pore space is below the resolution of the images, but larger structural changes such as the variations in bedding plane orientation and the relative frequency of higher density materials can be observed. With these images brighter areas of the scan indicate higher x-ray attenuation, which indicates higher density areas. Fractures in the core can be observed as dark regions, due to the low x-ray attenuation of the air in these openings.
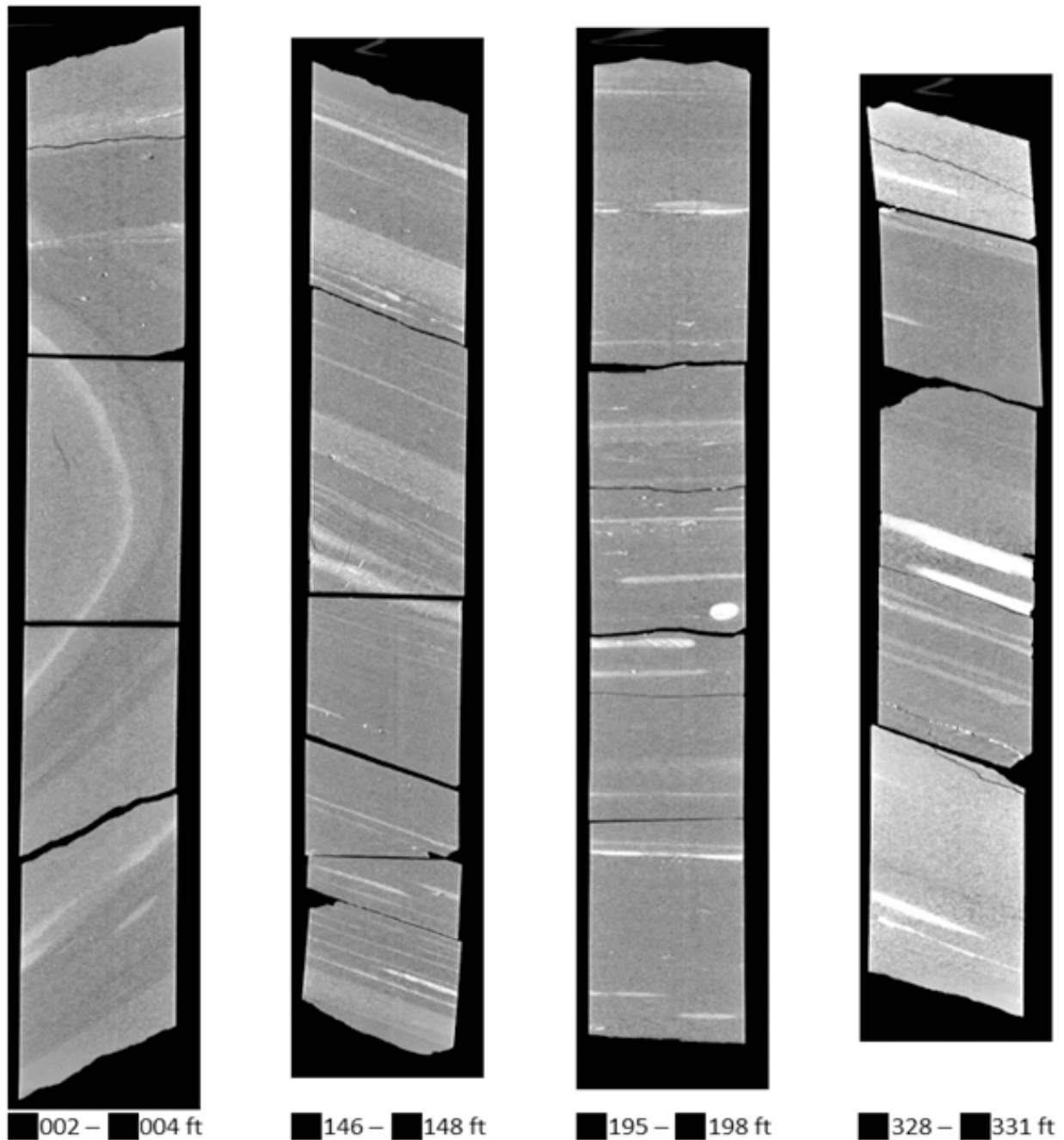

■002 – ■004 ft   ■146 – ■148 ft   ■195 – ■198 ft   ■328 – ■331 ft

Figure 5: Representative medical CT images along the length of the Caney shale core

Higher resolution CT images of selected sections and regions of interest are also described by Paronish et al. (2021) and available on NETL's EDX. An example of these images is shown in Figure 6(a), where cross-sections through the center of an industrial CT scan with (32.9 mm)3 voxel resolution of a core plug are shown. At this higher resolution a void (black opening) is visible in the center of the sample, along with interspersed high density minerals throughout the matrix.

Similar results were obtained using an industrial CT scanner in the Hydraulic Barrier and Materials Characterization Laboratory at Oklahoma State University. Figure 6(b) shows a variation in bedding planes along the reservoir 1 sample and the heterogeneity of the shale matrix
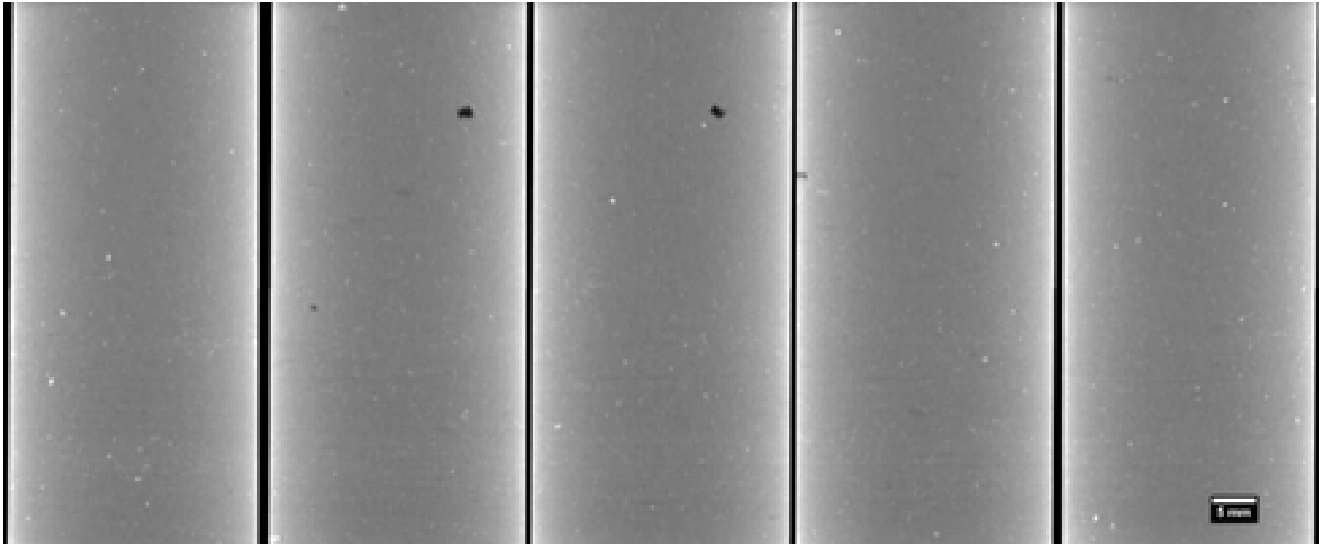
(a) 1×2-inch core plug representative of a reservoir section that are fairly homogeneous as depicted by monochromatic gray color
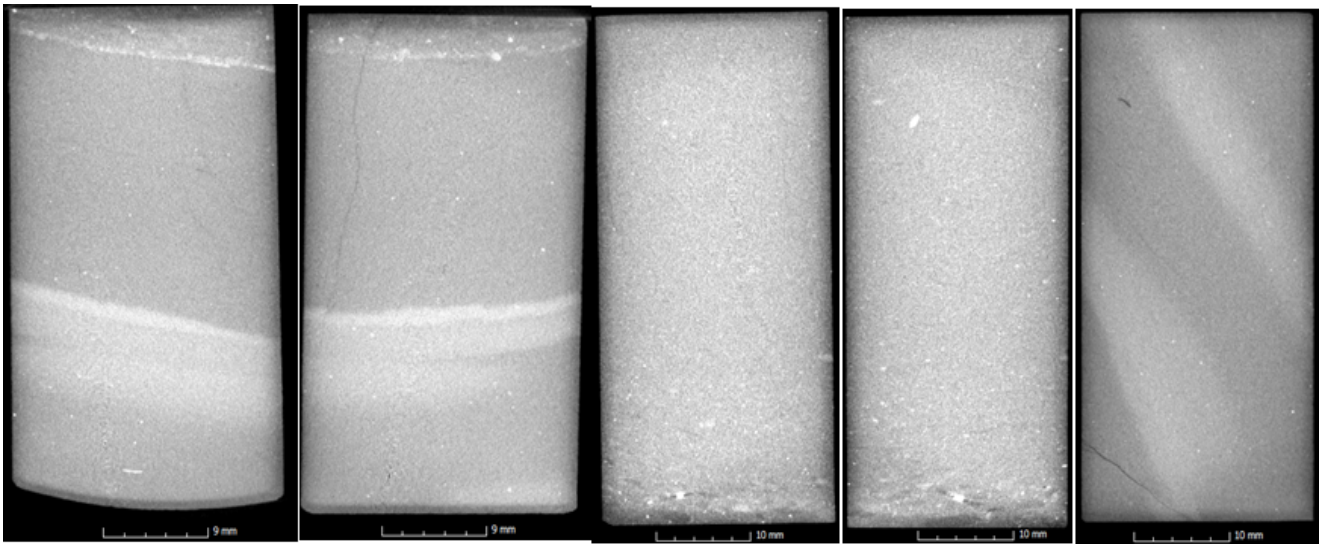
(b) Representative cores showing mineralogical heterogeneity within the Caney shale formation as depicted by bright regions rich in calcium, phosphates, and organic organic rich clay ductile regions are shown in Figure 6(a).

Figure 6: Montage of high resolution CT images through the center of 1×2-inch drilled core plugs from the 4-inch Caney shale core at different orientations to the bedding

X-ray Fluorescence (XRF) The full suite of geophysical data collected along the length of the core and described in Paronish et al. (2021) is available on NETL's EDX. This data was collected using the Multi-sensor Corelogger at NETL. XRF was run using a the Innov-X® X-Ray Fluorescence Spectrometer. This data is available in processed and raw formats, and with minimal processing for additional analysis. Two compiled logs of these data streams along the length of core are shown in Figures 7 and 8. Figure 7 combined the gamma density, medical CT images, magnetic susceptibility along with the elemental counts from the handheld XRF that was measured every 6 cm. Figure 8 combines some of these tracks with elemental mineralogy where Ca contributes to carbonate minerals, Al represents clay minerals, and Si is assumed to contribute to quartz; and important elemental ratios from the XRF (Si/Al, Ca/Si, Mn/Fe, Fe/Al, S/Fe, and Ti/Al) which can provide insights into the depositional state of the formation (Paronish et al., 2021). Si/Al, can provides information on the abundance of illite and micas versus other clays; Ca/Si, provides information on relative abundance of calcium carbonates versus silicates; Mn/Fe, provides information on oxidation, where a decrease in the ratio is related to zones of anoxic/euxinic conditions and an increase is related to zones of dysoxic/oxic conditions; Fe/Al, which provides information about the degree of pyritization in shales; S/Fe, which provides information on the abundance of pyrite (and other iron sulfates) versus Fe oxide minerals; and Ti/Al, which provides information about terrigenous input.
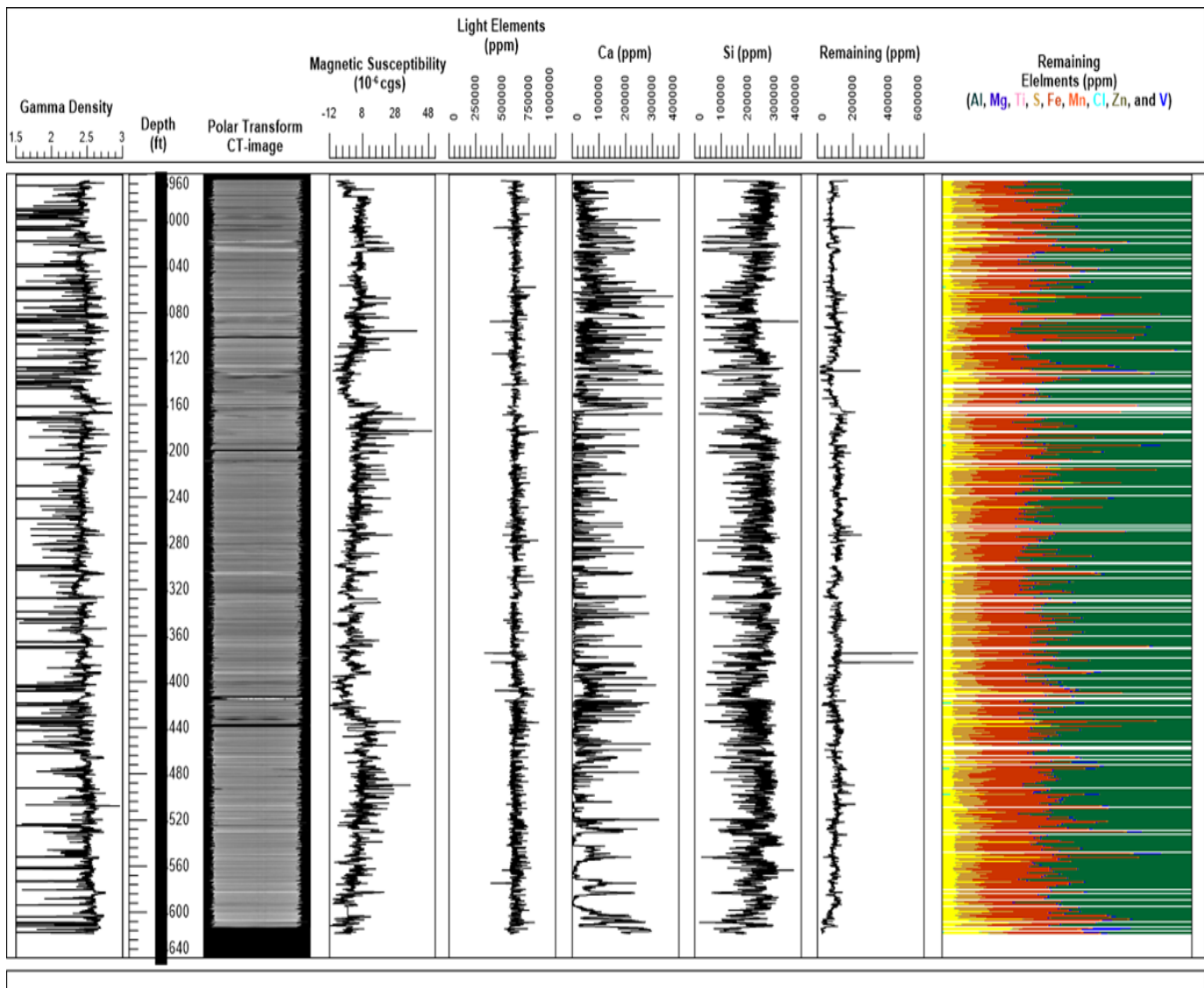

Figure 7: Stacked bar graph showing initial mineralogical compositions of samples used in experiment. Mineralogy of samples are generally the similar with variations showing mainly in the percentage composition of individual minerals.
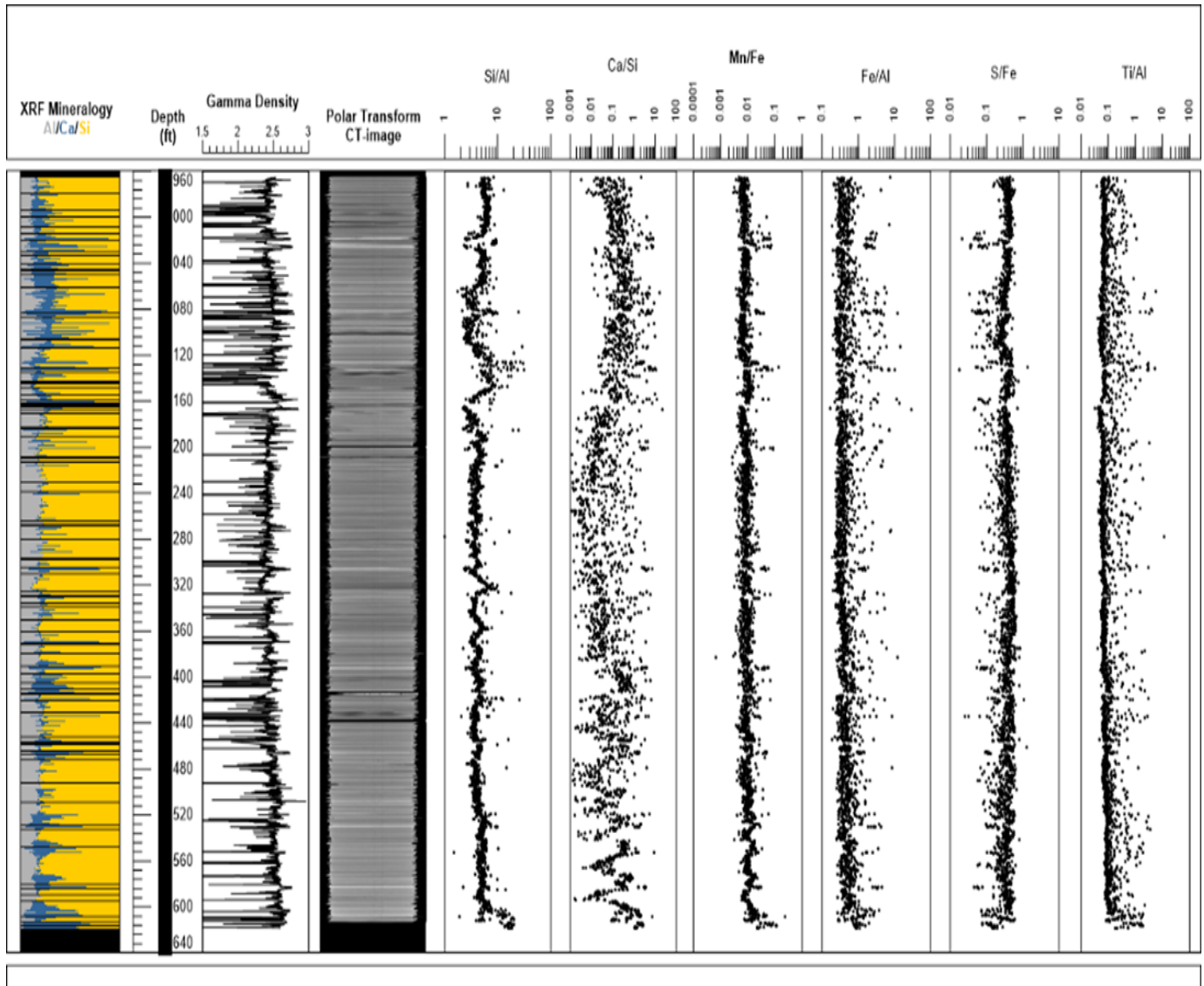
Figure 8: Log of high resolution geophysical measurements and ratios of XRF elements of the Caney shale core.

Total Organic Carbon (TOC) To understand the quality of organic matter, a plot of remaining hydrocarbon potential versus total organic carbon is used. Figure 10 shows that the Reservoir 1 sample has Type II organic matter and it is oil prone whereas; Ductile 1, Ductile 2, Reservoir 2 and Reservoir 3 show Type III organic matter and they are gas prone. Overall from Figure 10, we can conclude that Caney shale samples used in this study are mature.

X-ray Diffraction (XRD) Samples are composed of similar mineralogical compositions, but the variations are observed in the quantities of minerals in each sample (Figure 9). This points to a common provenance for samples which experienced different depositional conditions and environments. Samples are predominantly quartz, feldspar, carbonate and illite with minor pyrite compositions. Average weight % composition of 'quartz + feldspar + pyrite' for sample 1 to sample 5 are 64.7%, 64.7%, 72.7%, 79% and 72.3% respectively. Carbonates showed compositions of 12.3%, 6.1%, 4.9%, 0% and 16.9% whilst clay minerals were 23%, 29.2%, 22.4%, 21% and 10.9% samples A, B, C, D and E respectively.
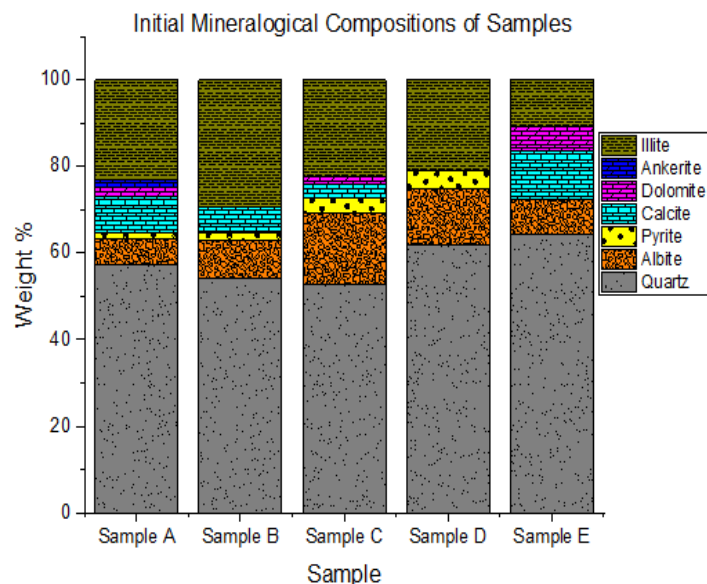

Figure 9: Stacked bar graph showing initial mineralogical compositions of samples used in experiment. Mineralogy of samples are generally the similar with variations showing mainly in the percentage composition of individual minerals.
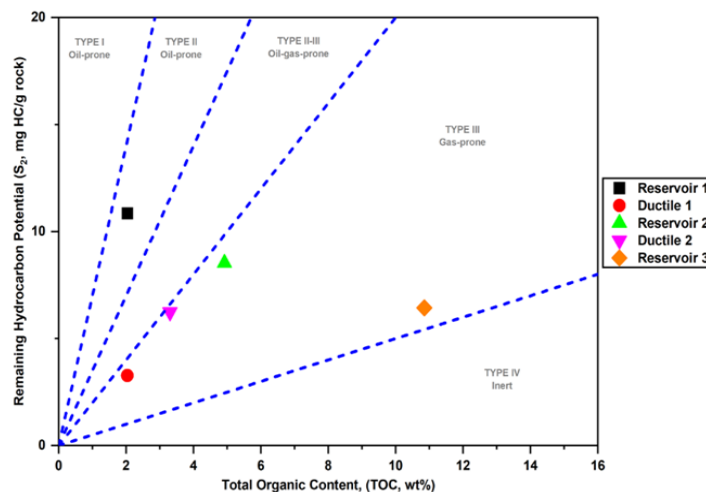

Figure 10: A plot showing the relationship between remaining hydrocarbon potential and total organic carbon. The figure shows that Caney shale samples are within Type II and Type III organic matter and are mature.

Porosity/Permeability Porosity and permeability of the samples were determined. Figure 11 shows the results obtained from porosity and permeability testing. From figure 11, porosity varied from 2.8% in Ductile 1 to 3.6% in Reservoir 3. Reservoir 2 and Ductile 2 samples had the same porosity measurements of 3.2%. Figure 11(b) shows the comparison between permeability measured from as received samples and permeability measured on samples that were cleaned using Carbondioxide (CO_2) or Toluene($C_6H_5CH_3$). Results in Figure 11(b) show that overall permeability of the Caney shale samples is low. However, when samples were cleaned with Carbondioxide (CO_2) or Toluene($C_6H_5CH_3$), permeability increased slightly but the magnitude of the overall permeability was still in nano-Darcy(nD).
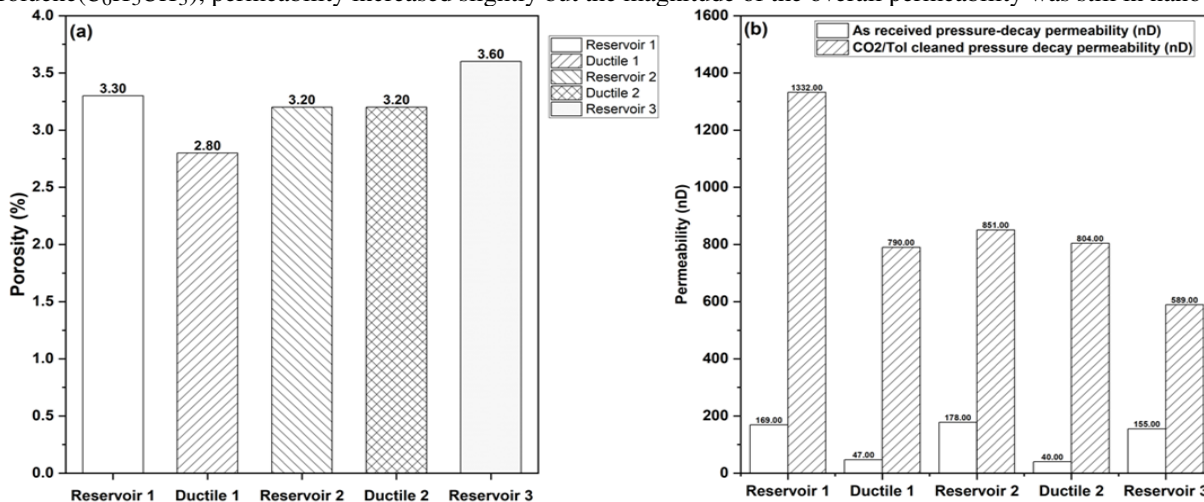

Figure 11: (a) Porosity of the samples under investigation (b) Permeability of the samples under investigation: The porosity data indicates that the porosity of the samples is very low with values ranging from 2.8% in Ductile 1 to 3.6% in Reservoir 3.

Microstructure: Scanning Electron Microscopy and Energy Dispersive Spectroscopy (SEM/EDS) Several types of mixed carbonate-siliciclastic facies were identified in core, including mudstone, siltstone, to carbonate facies (Figure 12). These facies show variabilities in mineralogy (bulk clay, quartz, carbonate), grain type and size, and sedimentary structures.
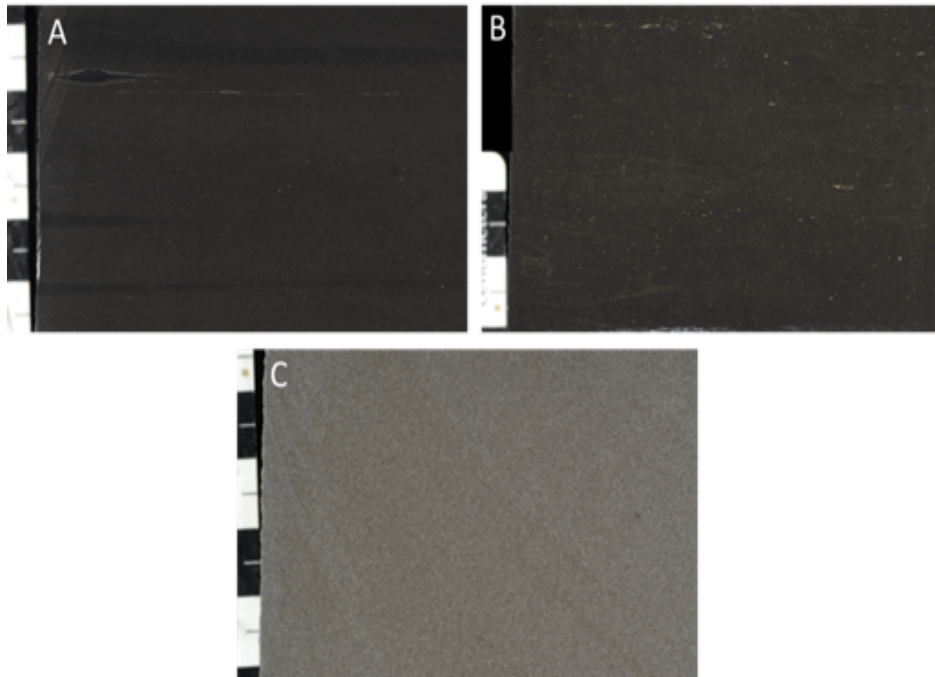

Figure 12: The Caney core utilized in this study contains several types of mudstone (A), siltstone (B), and carbonate (C) facies. All photos are taken from core samples. Scales in photos are in centimeters
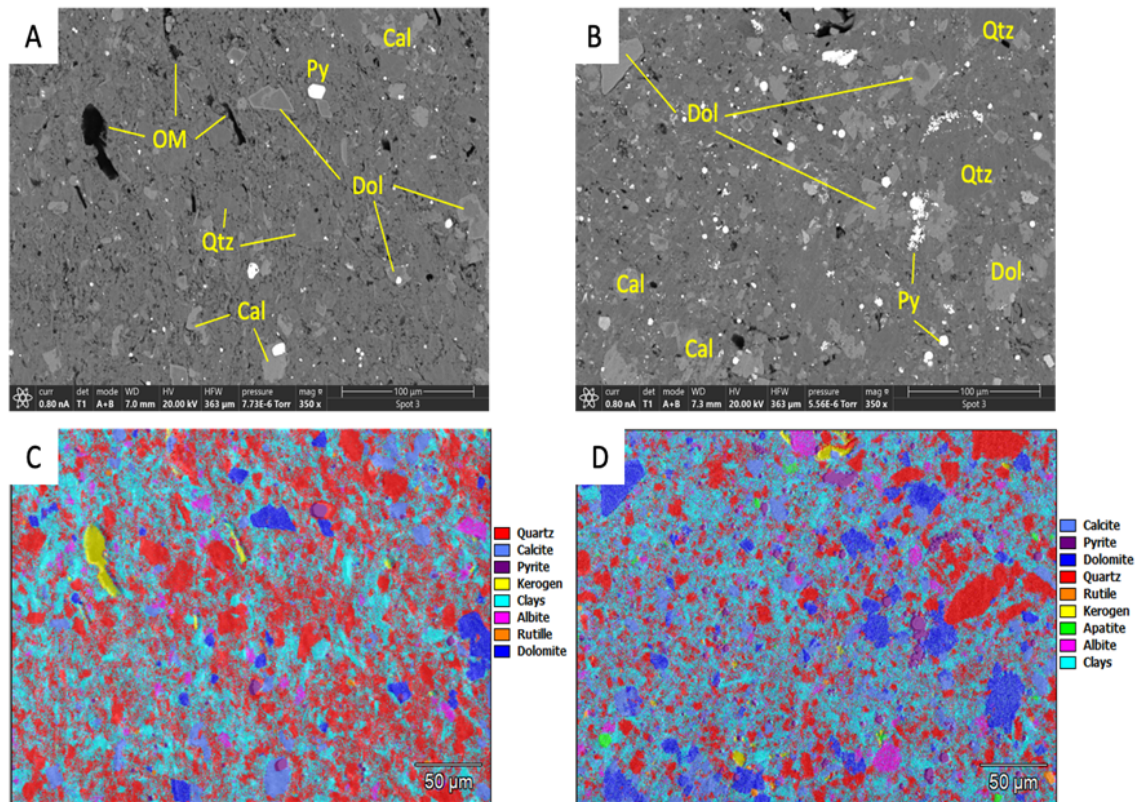

Figure 13: SEM images and EDS phase maps of brittle (Reservoir 1, A and C) and ductile (Ductile 1, B and D) Caney shale samples. A shows a higher heterogeneity of inorganic mineral particles than B, as suggested by C and D. C shows a higher average particle size for brittle sample than D, the ductile sample. OM: organic matter. Dol: dolomite. Cal: calcite. Py: pyrite. Qtz: quartz.

Figure 13 shows that for the brittle Caney shale R1 sample, the average inorganic mineral particle size is 20μm, which is higher than that of the ductile D1 sample, 5-10μm. In other words, the ductile D1 sample is of finer matrix particles than the brittle R1 sample. Another feature of R1 sample is a higher content of quartz than D1 sample, which contributes to a higher heterogeneity of matrix-related geochemistry and mineralogy.
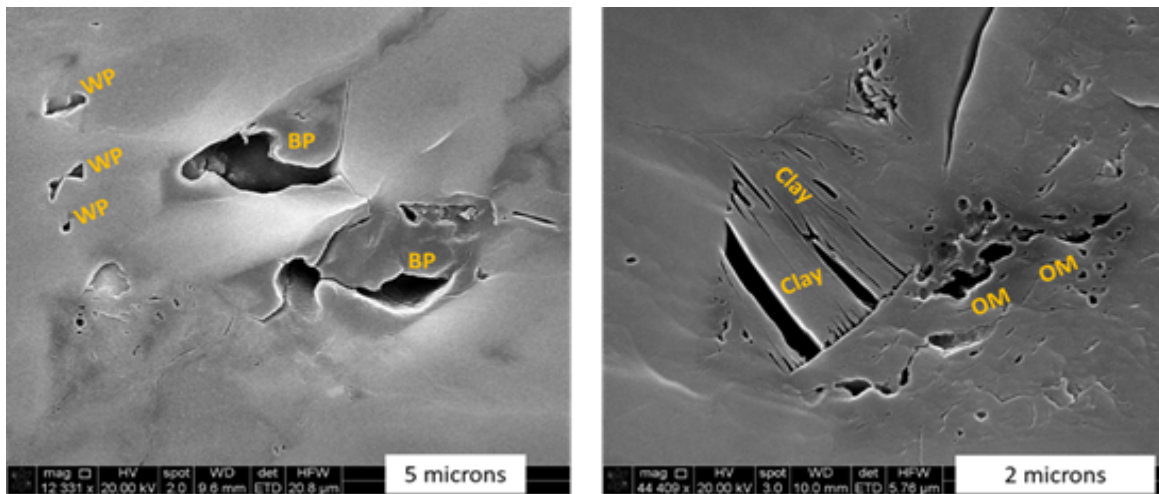

Figure 14: Based on SEM imaging of selected samples, common pore types include intraparticle (WP), interparticle (BP), organic matter (OM), and pores hosted by clay minerals (Clay).

Because the pores of this study are nanometer to micron in size, scanning electron microscope (SEM) is utilized to analyze the pore systems. Some of the common pore types include intraparticle (WP in Figure 14), interparticle (BP in Figure 14), organic matter pores (OM in Figure 16), and pores hosted by clay minerals (Clay in Figure 14).

Mechanical properties

Creep testing Results from creep testing revealed a significant difference in creep compliance between the nominally more ductile zones and the nominally more brittle reservoir zones. As shown in Figure 15, the ductile zones have higher creep compliance after 72 hours of loading time compared to the reservoir zones. Note these values are the predicted compliance based on the power-law fit (see Benge et al. (2021) for additional information and discussion).

This increased value of creep compliance for the ductile zones is present in both the vertical and horizontal samples. While the creep compliance does not appear to be isotropic, the trends holding for both the vertical and horizontal orientations indicates the relative tendency to creep remains the same regardless of bedding plane direction. The increased tendency to creep also corresponds to greater long term deformation of the ductile samples. An investigation into the influence of the long-term deformation with respect to fracture closure and proppant embedment is discussed by Benge et al. (2021). Additional factors which are influenced by the differences in creep values for the different zones include the eventual changes in stresses as the formations relax to a more geostatic stress state (see for example Sone and Zoback (2014)).
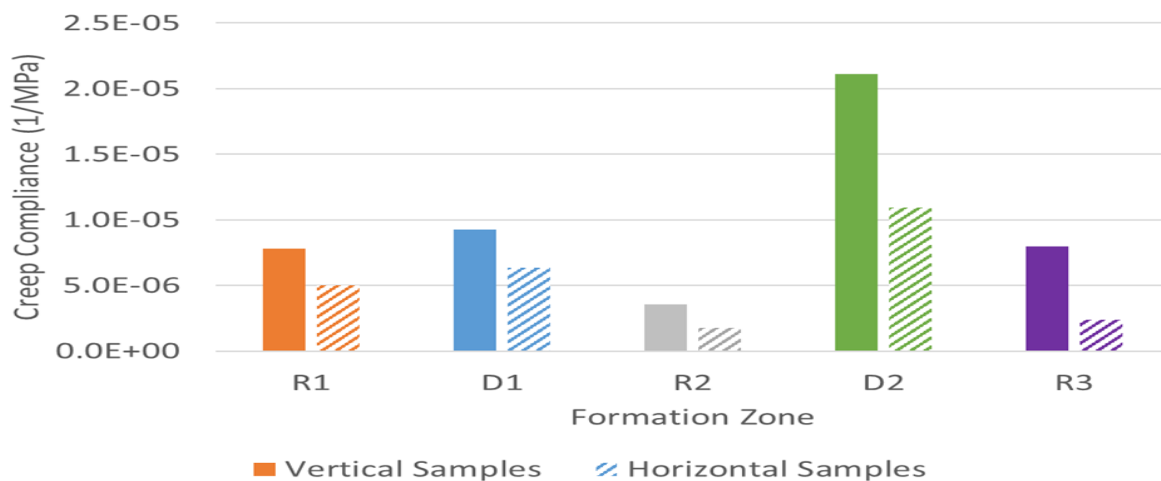

Figure 15: Predicted creep compliance after 72 hours of creep testing for vertical and horizontal samples showing a general trend to higher creep in the nominally ductile zones compared to the reservoir zones and higher creep in the vertical direction compared to the horizontal direction.

In-situ fluorescence visualization(ISFV) of proppant and fracture aperture evolution Some of the images obtained during a 2-week compaction experiment are shown in Figure. 16, and the initial primarily stress-dependent deformations and later, long-term creep deformations in Figure. 17. The temperature of the experiment was 122°C, effective compaction stress 27 MPa, and the fluid pressure 10.4 MPa. The fluid used with the sample was synthetic brine, containing 4.7% NaCl, 0.17% MgCl$_2$, 0.076% CaCl$_2$, and 0.028% SrCl$_2$ by weight (except for NaCl, all are hexahydrate salts). In spite of the shale's high clay content, a severe level of proppant crushing was observed during the initial loading, although most of the cracked grains seem to be still holding the load, as indicated by the dark shadows of the grains made by the contact between the proppant grain surfaces and the view window. The images indicate that although the proppant crushing stopped once the target stress was reached, a small number of the grains still continued to crush. The crushing of the proppant however was also accompanied by brittle fracturing of the shale matrix, which caused some embedment of both crushed and intact proppant grains. This was confirmed by examining the shale sample surface after the experiment (Figure. 18). This process of mutually destructive proppant-shale interaction would be producing fines from both proppant and shale matrix, which may have a significant impact on the reservoir permeability, if they migrate and accumulate at proppant pack pore throats and narrowed apertures of fractures.
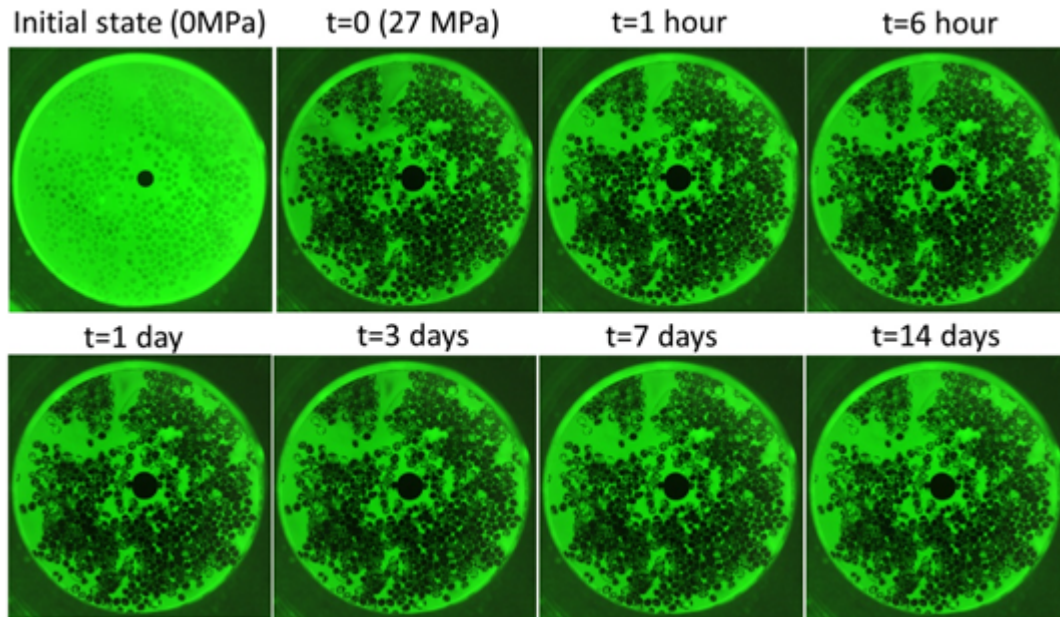

Figure 16: Time-lapse fluorescence images of a Caney shale disc with proppant subjected to effective compaction stress of 27MPa in brine at 122oC. The black center circle is a Viton disc that was used to determine the actual aperture changes of the fracture from images independently from LVDT measurements.
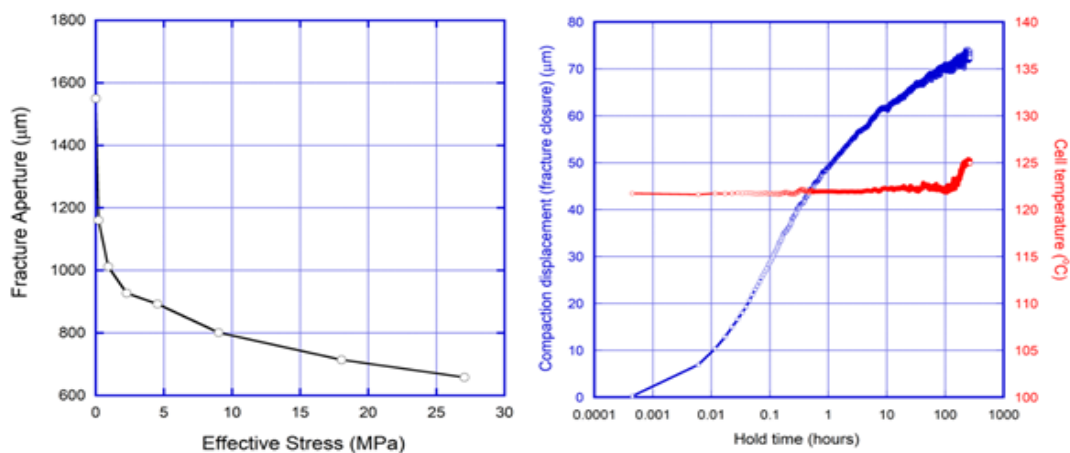

Figure 17: Stress dependent initial closure (a) and long-term creep closure (b) of an analogue shale fracture. Initial closure is mostly due to the elastic deformation and crushing of the proppant grains. Long-term closure is primarily caused by slow embedment of the proppant grains into the shale matrix (Katende et al., 2023a).

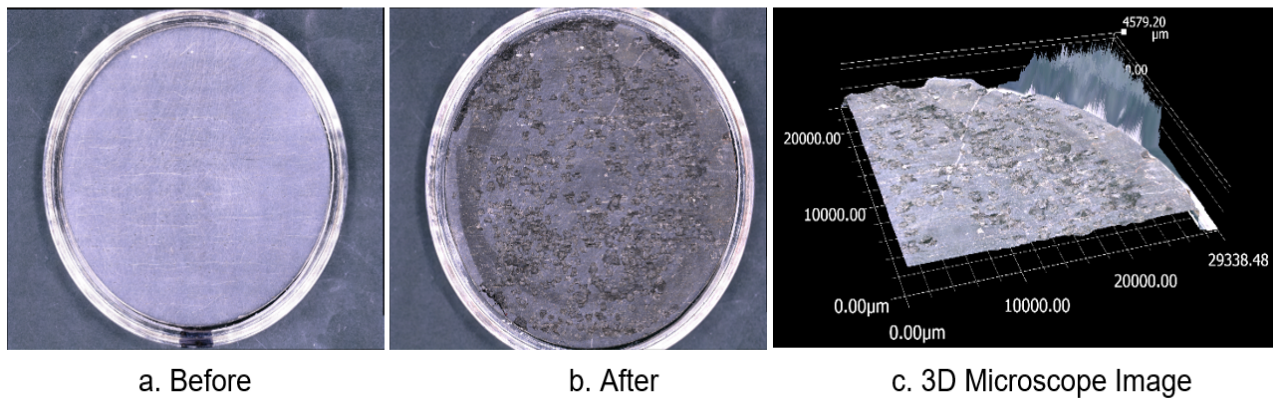a. Before   b. After   c. 3D Microscope Image

Figure 18: A Caney shale disc used for the ISFV experiment. Comparison of the images before (a) and after (b, c) the long-term compaction experiment reveals severe shale matrix damage caused by proppant indentation. Rather than plastic deformation that would cause heaving of the shale around the proppant casts, the observed damage involved microfracturing and debris formation.

Indentation testing Figure 19 shows a plot of the relationship between hardness and elastic modulus for the samples tested using Micro-Indentation. From Figure 19, we can see that Hardness and Elastic Modulus across the five samples tested varies. Ductile samples had the least hardness and elastic modulus with Ductile 2 having a hardness of 0.5GPa and an Elastic Modulus of 16GPa. Reservoir samples in general exhibited the highest hardness and elastic modulus. Since proppant embedment occurs on the surface, a lower hardness would imply that such samples are more susceptible to proppant embedment compared to samples with a higher hardness.
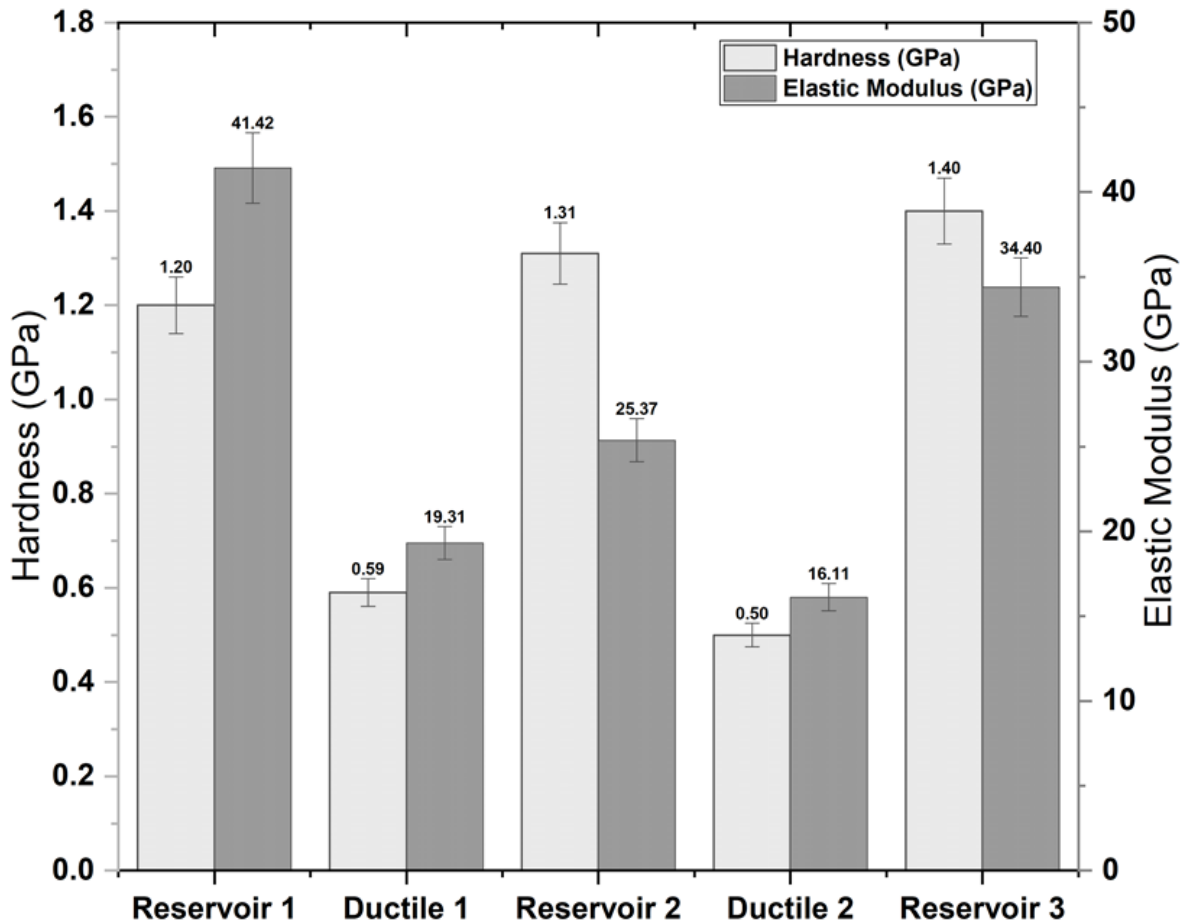

Figure 19: A plot of Hardness and Elastic Modulus of the samples tested with indentation. The figure shows that hardness and elastic modulus vary across all the samples. Ductile 2 exhibited the lowest hardness and elastic modulus whereas reservoir 1 had comparably higher values of hardness and elastic modulus.

API fracture permeability versus monolayer fracture permeability Results from an American Petroleum Institute standard fracture permeability testing protocol (Katende et al., 2023a) are compared to laboratory tests of fracture permeability using monolayer proppant (Katende et al., 2023b) in Figure 20. From Figure 20, we can see that the Caney shale composite with monolayer proppant has significantly lower fracture conductivity compared to API standard test with multilayer proppant. From Figure 20, it is clear that as the confining stress increases, fracture conductivity decreases but the loss in fracture conductivity for monolayer proppant is much faster compared to a multi-layer propped fracture which is more representative of a field fracturing scenario.
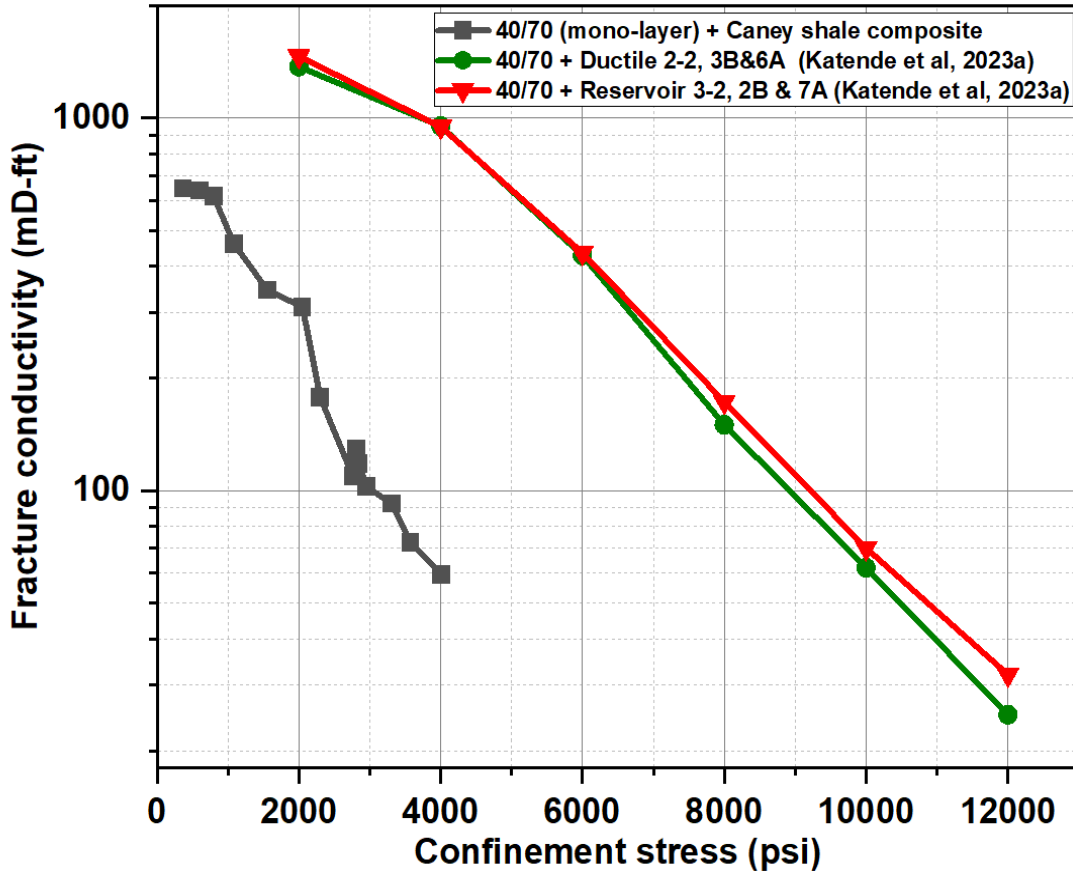

Figure 20: A plot showing the relationship between fracture conductivity and confining stress for the monolayer propped fracture and multi-layer propped fracture from standard fracture conductivity test.

Long term modeling of fracture permeability For geomechanical modeling of long-term fracture permeability, the FLAC3D ubiquitous joint model is used, considering the isotropic strength of the matrix rock as well as shear and tensile strength of weak planes with given orientations. In this case, we orient the weak planes in the ubiquitous joint model along a local fracture trace so that shear failure and tensile failure would only be initialized for the local fracture orientation. This model is general so that it can also work for proppant filled fractures, as illustrated in Figure 21. This model of closure including creep embedment can also be applied to an equivalent fracture material. The parameters for a 5-cm thick equivalent fracture model were calibrated to achieve a time dependent function of permeability reduction in terms of a permeability change factor. This model of permeability reduction was applied to the modeling of production as described below.
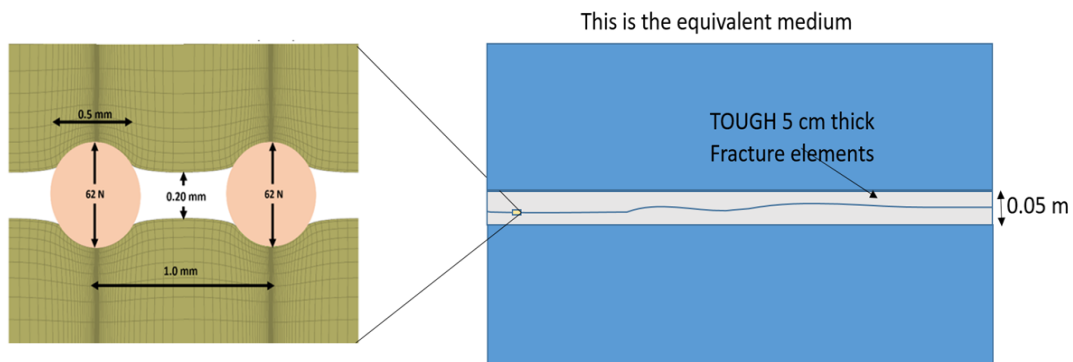

Figure 21: Concept of creep embedment (left) to a finite thickness equivalent fracture model (right) that can be conveniently applied in the numeral simulation of gas production.

Production modeling of a generic site based on the Caney Shale includes brittle and ductile layers in the reservoir, and fracture permeability reduction due to creep compaction using a time-dependent permeability function. The basic conceptual model consists of methane production from a horizontal well intercepting a single planar vertical fracture (the primary fracture), which is surrounded by a stimulated reservoir volume (SRV) consisting of a network of secondary fractures, divided into brittle and ductile layers. Beyond the SRV, permeability is assumed to be negligible.

Figure 22 shows the production decline curve when the permeability reduction factor is applied to various materials: the primary fracture, the ductile part of the SRV, the brittle part of the SRV, and the entire SRV. When permeability of the primary fracture is reduced, the production decline curve does not change at all. This is because the primary fracture supplies gas only during very early times, before the fracture permeability has declined significantly. When permeability of the ductile layer is reduced, the production rate does not change until about two years, because the low original permeability in the ductile layer means it only supplies gas after other parts of the system are exhausted. When permeability of the brittle layers is reduced, the production rate change starts earlier, after only a few months, because after the quick exhaustion of the primary fracture, it is the main supplier of gas. When the permeability of both ductile and brittle layers is reduced, the production rate starts early and continues a long time, reflecting both the individual effects. If we consider the 10-year production rate of the constant-permeability case as a lower limit for useful production rate, Figure 22 shows that it is reached much sooner, within 8 years, for the reduced permeability case.
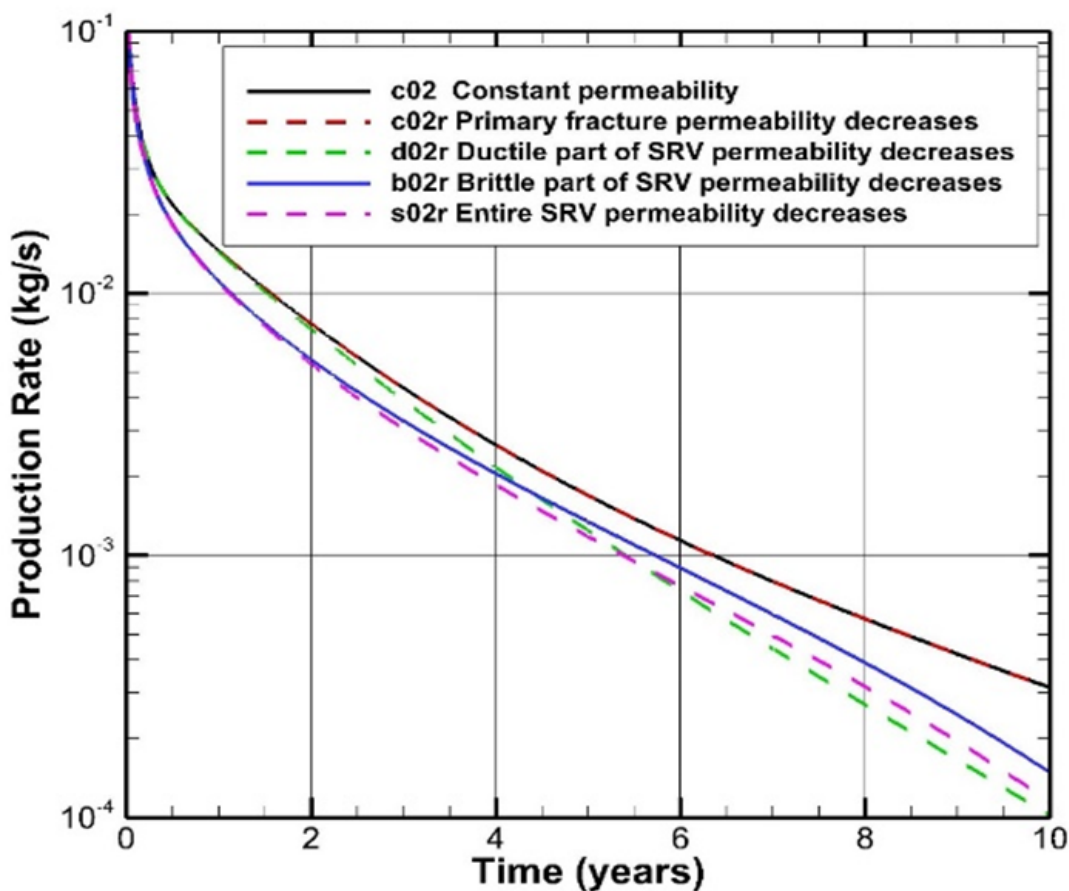

Figure 22: Production decline for permeability reduction in different materials of the model.

Production Production data indicate the Caney Shale produces economically from brittle reservoir intervals. Three different reservoir intervals have been completed upper Reservoir 3, lower Reservoir 3 and Reservoir 2. The well completed in upper Reservoir 3, which has the shortest lateral (≈5800 feet), had a cumulative production after 12 months of 43,200 barrels of oil and 199, 984 thousand cubic feet (MCF)gas and average production rate of 100 BOPD and 523 MCF gas per day. The well completed in lower Reservoir 3 cumulated 110, 718 barrels of oil and 547, 290 MCF gas after 12 months, with average production of 195 barrels of oil per day(BOPD) and 1168 MCF gas per day. The third well, which is completed in 9600 feet long lateral in Reservoir 2, cumulated 111, 561 barrels of oil and 331,208 MCF gas after 12 months and produced an average of 186 BOPD of oil and 580 MCF gas per day.

Discussions

Caney shale at reservoir/wellbore scale: log data The changing elemental concentrations and their respective wireline log characteristics reflect changes in mineralogy (Figure 4). Interval 1 with increasing Ti, Zr and Al concentrations in combination with decreasing Si concentration, is a clay-rich interval. Al in mudrocks like the Caney Shale is mostly from aluminosilicate clay minerals that are abundant in interval 1. Ti and Zr are associated with detrital quartz silt. Because Si concentration decreases in interval 1 while Ti and Zr increase, the detrital sediment that is rich in clay minerals is seemingly deficient in Si that is expected with increasing quartz silt. In interval 2, Si increases at the same time the terrigenous indicators Ti, Zr and Al are decreasing. This relationship supports the hypothesis of a non-detrital source for Si that causes the increased concentration in Si as the concentrations of the detrital indicators decline. Interval 3 with simultaneous increasing Ti, Zr, Al and Si reflects an influx of clay-mineral rich and detrital-quartz-silt rich sediment. Because clay-mineral content is still high and as a result bound water content is high, the rock exhibits lower resistivity and high neutron porosity. Likewise, the abundance of clay minerals in interval 1 causes low resistivity and high neutron porosity. In interval 2 with its lower Al concentration resulting from lower clay mineral content, resistivity increases, and neutron porosity decreases. Density porosity is believed to increase in interval 3 as a result of increased gas and/or organic matter content. Interval 4 that is rich in Ca is carbonate has minimal clay mineral or quartz silt content. As a result, the concentrations of Ti, Zr, Al and Si are low and neutron porosity is low in response to low clay mineral concentrations. Uncorrected density porosity is also very low in response to calcite cement that occludes pores and reduces porosity to near zero porosity units.

Those intervals with increased Si content and decreased clay-mineral content are brittle and susceptible to natural fracturing and hydraulic fracturing during completion. These intervals are evident on open-hole wireline logs as having lower neutron porosity, higher density porosity and higher resistivity. In contrast, those intervals that are richer in clay-minerals as indicated by higher neutron porosity and lower density porosity and lower resistivity are ductile zones that serve as seals and possible barriers to hydraulic fractures

Caney shale depositional setting, pore types, natural fractures and microstructure The facies identified from core are interpreted to represent lower-energy background sedimentation (e.g., suspension settling; mudstone-siltstone) and higher-energy event deposition (e.g., turbidity current; carbonate), corresponding to different environments on a distally steepened ramp system. The pore types documented in this study (Figure 12) are observed in most of the Caney facies identified in core. There seems to be differences in the relative abundance of these pore types in different facies, which can be related to the different mineralogy and grain types among facies. As further indicated by its higher rebound hardness values, the carbonate facies can potentially be considered as favorable targets for hydraulic fracturing. As such, integrating facies with reservoir properties can assist in reservoir characterization and production design.

The differences of geochemistry and microstructure between the ductile and brittle shale sample may account for the different geomechanical behaviors under stress and different performance of fracture permeability. For the brittle shale, a higher content of rigid quartz particle with a higher average particle size is more prone to be fractured and resist closure, compared to the finer and softer ductile shale. After applied stress, proppant embedment is more readily observed within the ductile shale due to a higher content of flexible clays within the matrix. In addition, a higher content of clays within the ductile shale matrix results in a higher deformation, compared to the brittle shale. This phenomenon was supported by the creep tests and modeling.

Laboratory to field correlation In unconventional reservoir development, hydraulic fracturing design plays a major role in the capital costs, well performance, and profitability of unconventional reservoirs, and thus the optimization of the completion design must take these parameters such as proppant embedment and its influence on fracture conductivity into consideration. Crucially, the completion optimization plan should be robust and based on the detailed testing of the different formations throughout the area. For example, parts of the reservoir are likely to not be stimulated if the completion design is insufficient for a given spacing and there is not enough proppant. As the proppant cost is significant in well completion in hydraulic fracturing, operators tend to choose low-cost proppants such as silica quartz sand one of the cheapest and most accessible proppants. However, it should be noted that the use of proppants that increase the fracture conductivity such as ceramic coated proppants are more likely to generate higher performance in the long term but are very expensive and unfeasible in field development.

Besler et al. (2007) observed that long-term production was sustained from wells where ceramic proppants were used as compared to conventional sand implying that the type of proppants used can significantly affect production.

Conclusions

In this paper, we have utilized a multidimensional, experimental and modeling evaluation of permeability evolution of the Caney shale field lab in Oklahoma and the following conclusions can be drawn.

1. The outcomes of the micro-indentation revealed variations in mechanical properties attributed to changing mineral composition and microstructures.

2. Outcomes from API fracture conductivity testing and flow- through testing using a monolayer of proppant demonstrated:
    (a) a 50% impact on proppant embedment compared to ductile samples
    (b) a significant decline in fracture conductivity with increasing stress and temperatures,
    (c) and conductivity was also influenced by organic and inorganic content as well as internal sample architecture.

3. Mineralogically, ductile samples contain about 25% more clay minerals compared to brittle regions. Heterogeneity in mineral composition causes the Caney Shale to show different responses at reservoir temperature and pressure, particularly in relation to creep and proppant embedment.

4. The outcomes from this integration should aid geological and engineering predictions for the hydrocarbon production and caprock integrity of the Caney Shale.

Acknowledgements

Nomenclature

$J =$	Creep compliance
$\varepsilon =$	Strain
$\sigma =$	Differential stress
$t =$	Time
$B =$	Creep scalar value
$KCl =$	Potassium Chloride
$AFS =$	Automated Core Flooding System
$API =$	American Petroleum Institute
$HCl =$	Hydrochloric Acid
$TOC =$	Total Organic Carbon
$EDS =$	Energy Dispersive Spectroscopy
$SEM =$	Scanning Electron Microscopy
$mA =$	milli Ampere
$kV =$	kilo Volts
$CO_2 =$	Carbondioxide
$FiB =$	Focussed Ion Beam
$R1 =$	Reservoir 1
$D1 =$	Ductile 1
$R2 =$	Reservoir 2
$D2 =$	Ductile 2
$R3 =$	Reservoir 3
$UV =$	Ultra Violet
$BOPD =$	Barrels of Oil per Day
$SRV =$	Stimulated Reservoir Volume
$ISFV =$	In-situ Fluorescence Visualization
$FEP =$	Fluorinated Ethylene Propylene
$LVDT =$	Linear Variable Differential Transformer

Superscripts

$n =$	data assimilation step number

References

Algeo, T. J. and Maynard, J. (2004). Trace-element behavior and redox facies in core shales of Upper Pennsylvanian Kansas-type cyclothems. *Chemical Geology*, 206:289–318.

Andrews, R. D. (2007). Stratigraphy, Production, and Reservoir Characteristics of the Caney Shale in Southern Oklahoma. *The Shale Shaker*, 58(1):9–25.

Awejori, G. A., Luo, G., Grider, C., Katende, A., Radonjic, M., Doughty, C., Spycher, N., Paronish, T., O'Connell, L., and Rihn, A. (2021). Fracturing Fluid-Induced Mineralogy Changes and Impact on Elastic Properties for the Caney Shale, Oklahoma. pages 1–7. Paper presented at the 55th U.S. Rock Mechanics/Geomechanics Symposium, Virtual, June 2021.

Benge, M., Lu, Y., Katende, A., Rutqvist, J., Crandall, D., Haecker, A., King, G., Renk, J. B., Radonjic, M., and Bunger, A. (2021). Connecting Geomechanical Properties with Potential for Proppant Embedment and Production Decline for the Emerging Caney Shale, Oklahoma. pages 1–13. Paper presented at the SPE/AAPG/SEG Unconventional Resources Technology Conference, Houston, Texas, USA, July 2021. Paper Number: URTEC-2021-5084-MS.

Besler, M. R., Steele, J. W., Egan, T., and Wagner, J. (2007). Improving Well Productivity and Profitability in the Bakken?A Summary of Our Experiences Drilling, Stimulating, and Operating Horizontal Wells. pages 1–13. Society of Petroleum Engineers, SPE Annual Technical Conference and Exhibition held in Anaheim, California, U.S.A., 11?14 November 2007.

Cardott, B. J. (2017). Oklahoma Shale Resource Plays. *Oklahoma Geological Survey*, pages 1–10.

Clarkson, C., Solano, N., Bustin, R. M., Bustin, A., Chalmers, G., He, L., Melnichenko, Y., Radlinski, A., and Blach, T. (2013). Pore structure characterization of North American shale gas reservoirs using USANS/SANS, gas adsorption, and mercury intrusion. *Fuel*, 103:606–616.

Clarkson, C. R., Jensen, J. L., and Blasingame, T. (2011). Reservoir Engineering for Unconventional Reservoirs: What Do We Have to Consider? pages 1–45. Society of Petroleum Engineers, North American Unconventional Gas Conference and Exhibition, 14-16 June, The Woodlands, Texas, USA.

Ding, W., Li, C., Li, C., Xu, C., Jiu, K., Zeng, W., and Wu, L. (2012). Fracture development in shale and its relationship to gas accumulation. *Geoscience Frontiers*, 3(1):97–105.

Dou, F., Wang, J. G., Wang, H., Hu, B., and Li, C. (2019). Discrete Element Analysis for Hydraulic Fracture Propagations in Laminated Reservoirs with Complex Initial Joint Properties. *KSCE Journal of Civil Engineering*, pages 1–23.

Guo, T., Zhang, S., Ge, H., Wang, X., Lei, X., and Xiao, B. (2015). A new method for evaluation of fracture network formation capacity of rock. *Fuel*, 140(2):778–787.

Guo, W., Shen, W., Li, X., Wang, N., Liu, X., Zhang, X., and Zhou, S. (2019). Study on mechanical characteristics and damage mechanism of the Longmaxi Formation shale in southern Sichuan Basin, China. *Energy Exploration & Exploitation*, 38(2):454–472.

Kamann, P. J. (2006). Surface-to-subsurface Correlation and Lithostratigraphic Framework of the Caney Shale (Including the "mayes" Formation) in Atoka, Coal, Hughes, Johnston, Pittsburg, and Pontotoc Counties, Oklahoma. Master's thesis, Oklahoma State University, Boone Pickens School of Geology 105 Noble Research Center Stillwater, OK 74078.

Katende, A., Allen, C., Rutqvist, J., Nakagawa, S., and Radonjic., M. (2023a). Experimental and numerical investigation of proppant embedment and conductivity reduction within a fracture in the Caney shale, Southern Oklahoma, USA. *Fuel*, 341.

Katende, A., O'Connell, L., Rich, A., Rutqvist, J., and Radonjic., M. (2021a). A comprehensive review of Proppant embedment in shale reservoirs : Experimentation, modeling and future prospects. *Journal of Natural Gas Science and Engineering*, 95:104143.

Katende, A., Rutqvist, J., Benge, M., Seyedolali, A., Bunger, A., Puckette, J. O., Rhin, A., and Radonjic, M. (2021b). Convergence of micro-geochemistry and micro-geomechanics towards understanding proppant shale rock interaction: A Caney shale case study in southern Oklahoma, USA. *Journal of Natural Gas Science and Engineering*, 96:104296.

Katende, A., Rutqvist, J., Massion, C., and Radonjic, M. (2023b). Experimental and numerical investigation of proppant embedment and conductivity reduction within a fracture in the Caney shale, Southern Oklahoma, USA. *Energy*, 273.

Lee, D. S., Herman, J. D., Elsworth, D., Kim, H. T., and Lee, H. S. (2011). A critical evaluation of unconventional gas recovery from the marcellus shale, northeastern United States. *KSCE Journal of Civil Engineering volume*, 15:679–687.

Liuke, H., Jianjun, L., Fengshou, Z., Dontsov, E., and Damjanac, B. (2019). Exploring the influence of rock inherent heterogeneity and grain size on hydraulic fracturing using discrete element modeling. *International Journal of Solids and Structures*, 176C177:207–220.

Loucks, R. G., Reed, R. M., Ruppel, S. C., and Hammes, U. (2012). Spectrum of pore types and networks in mudrocks and a descriptive classification for matrix-related mudrock pores. *AAPG Bulletin*, 96(2):1071 –1098.

Nakagawa, S. and Borglin, E. (2019). Laboratory In-Situ Visualization of Long-Term Fracture Closure and Proppant Embedment in Brittle and Ductile Shale Samples. pages 1–8. 53rd US Rock Mechanics/Geomechanics Symposium held in New York, NY, USA, 23-26 June 2019.

Oldenburg, C. M., Moridis, G. J., Spycher, N., and Pruess, K. (2004). TOUGH2 Module for Carbon Dioxide or Nitrogen in Natural Gas (Methane) Reservoirs . *EOS7C Version 1.0, Lawrence Berkeley National Laboratory, Berkeley, CA.*

Paronish, T. J., Mitchell, N., Schmitt, R., Brown, S. R., Crandall, D., Moore, J. E., Edelman, E., Esser, R., and McPherson;, B. (2022). Computed Tomography Scanning and Geophysical Measurements of State 16-2 Well in the Paradox Basin. *National Energy Technology Laboratory (NETL), Pittsburgh, PA, Morgantown, WV, and Albany, OR (United States).*

Paronish, T. J., Schmitt, R., Moore, J. E., Crandall, D., Rihn, A., Renk, J., Doughty, C., Bunger, A., Wang, Y., Katende, A., Seyedolali, A., Puckette, J., and Radonjic, M. (2021). Computed Tomography Scanning and Geophysical Measurements of the Caney Shale

Formation from the Tomaney# 1-35-34-27 Well. *National Energy Technology Laboratory (NETL), Pittsburgh, PA, Morgantown, WV, and Albany, OR (United States).*

Pruess, K. (2004). The TOUGH CodesA Family of Simulation Tools for Multiphase Flow and Transport Processes in Permeable Media. *Vadose Zone Journal*, 3(3):738–746.

Pruess, K., Oldenburg, C., and Moridis, G. (2012). TOUGH2 USER'S GUIDE. *Users Guide 2.0, Lawrence Berkeley National Laboratory, Berkeley, CA.*

Radonjic, M., Luo, G., Wang, Y., Achang, M., Cains, J., Katende, A., Puckette, J., Grammer, M., and King, G. E. (2020). Integrated Microstructural Characterisation of Caney Shale, OK. pages 1–18. Unconventional Resources Technology Conference.

Rutqvist, J. (2017). An overview of TOUGH-based geomechanics models. *Computers & Geosciences*, 108:56–63.

Rutqvist, J., Rinaldi, A. P., Cappa, F., and Moridis, G. J. (2013). Modeling of fault reactivation and induced seismicity during hydraulic fracturing of shale-gas reservoirs. *Journal of Petroleum Science and Engineering*, 107:31–34.

Sone, H. and Zoback, M. D. (2014). Viscous relaxation model for predicting least principal stress magnitudes in sedimentary rocks. *Journal of Petroleum Science and Engineering*, 124:416–431.

Tribovillard, N., Algeo, T. J., Lyons, T., and Riboulleau, A. (2006). Trace metals as paleoredox and paleoproductivity proxies: An update. *Chemical Geology*, 232:12–32.

Wang, Q., Chen, X., Jha, A. N., and Rogers, H. (2014). Natural gas from shale formation–The evolution, evidences and challenges of shale gas revolution in United States. *Renewable and Sustainable Energy Reviews*, 30:1–28.

Wang, Y., Luo, G., Achang, M., Cains, J., Wethington, C., Katende, A., Grammer, G. M., Puckette, J., Pashin, J., Castagna, M., Chan, H., King, G. E., and Radonjic, M. (2021). Multiscale Characterization of the Caney Shale-An Emerging Play in Oklahoma. *Midcontinent Geoscience*, 2:33–53.

Xu, S., Gou, Q., Hao, F., Zhang, B., Shu, Z., Lu, Y., and Wang, Y. (2020). Shale pore structure characteristics of the high and low productivity wells, Jiaoshiba shale gas field, Sichuan Basin, China: Dominated by lithofacies or preservation condition? *Marine and Petroleum Geology*, 114:104211.